

Ultracool Dwarfs Observed with the *Spitzer* Infrared Spectrograph. II. Emergence and Sedimentation of Silicate Clouds in L Dwarfs, and Analysis of the Full M5–T9 Field Dwarf Spectroscopic Sample

Genaro Suárez,^{1*} Stanimir Metchev,^{1,2}

¹Department of Physics and Astronomy, The University of Western Ontario, 1151 Richmond St, London, Ontario, N6A 3K7, Canada

²Institute for Earth and Space Exploration, The University of Western Ontario, 1151 Richmond St, London, Ontario, N6A 3K7, Canada

arXiv:2205.00168v1 [astro-ph.SR] 30 Apr 2022

Accepted XXX. Received YYY; in original form ZZZ

ABSTRACT

We present a uniform analysis of all mid-infrared $R \approx 90$ spectra of field M5–T9 dwarfs obtained with the *Spitzer* Infrared Spectrograph (IRS). The sample contains 113 spectra out of which 12 belong to late-M dwarfs, 69 to L dwarfs, and 32 to T dwarfs. Sixty-eight of these spectra are presented for the first time. We measure strengths of the main absorption bands in the IRS spectra, namely H₂O at 6.25 μm , CH₄ at 7.65 μm , NH₃ at 10.5 μm , and silicates over 8–11 μm . Water absorption is present in all spectra and strengthens with spectral type. The onset of methane and ammonia occurs at the L8 and T2.5 types, respectively, although ammonia can be detectable as early as T1.5. Silicate absorption sets in at spectral type L2, is on average the strongest in L4–L6 dwarfs, and disappears past L8. However, silicate absorption can also be absent from the spectra at any L subtype. We find a positive correlation between the silicate absorption strength and the excess (deviation from median) near-infrared colour at a given L subtype, which supports the idea that variations of silicate cloud thickness produce the observed colour scatter in L dwarfs. We also find that variable L3–L7 dwarfs are twice more likely to have above-average silicate absorption than non-variables. The ensemble of results solidifies the evidence for silicate condensate clouds in the atmospheres of L dwarfs, and for the first time observationally establishes their emergence and sedimentation between effective temperatures of ≈ 2000 K and ≈ 1300 K, respectively.

Key words: brown dwarfs — stars: atmospheres — infrared: stars

1 INTRODUCTION

Mid-infrared wavelengths (~ 5 – $50 \mu\text{m}$) sample prominent absorption features in the spectra of ultracool dwarfs, including water, methane, ammonia, and silicates (e.g. Roellig et al. 2004; Cushing et al. 2006;Looper et al. 2008), as predicted by diverse models (e.g. Burrows et al. 1997; Allard et al. 2001; Marley et al. 2002; Saumon et al. 2003). Prior to the *Spitzer* Space Telescope (Werner et al. 2004), these wavelengths remained spectroscopically unexplored in ultracool atmospheres. The Infrared Spectrograph (IRS; Houck et al. 2004) on *Spitzer* produced the first mid-infrared spectra of M, L, and T dwarfs (Roellig et al. 2004), and revealed prominent absorption bands of H₂O at 6.25 μm , CH₄ at 7.65 μm , and NH₃ at 10.5 μm . Cushing et al. (2006) and Looper et al. (2008) further noted the presence of strong silicate absorption between 9–11 μm in the spectra of four mid-L dwarfs. Subsequent studies have expanded the mid-infrared spectroscopic sample, for a total of 243 published spectra of \geq M5 dwarfs, of which 77 are field dwarfs (Roellig et al. 2004; Cushing et al. 2006; Saumon et al. 2007; Looper et al. 2008; Burgasser et al. 2008c; Leggett et al. 2009; Stephens et al. 2009; Kirkpatrick et al. 2010; Leggett et al. 2010b; Filippazzo et al. 2015; Suárez

et al. 2021) and 166 are members of young ($\lesssim 10$ Myr) stellar associations, namely Chamaeleon I, Coronet, η Chamaeleontis, Lupus, Ophiuchus, Serpens, Taurus, TW Hydra, and Upper Scorpius (Forrest et al. 2004; Apai et al. 2005; Furlan et al. 2005, 2006; Bouwman et al. 2006; Scholz et al. 2007; Luhman et al. 2007b; Merín et al. 2007; Morrow et al. 2008; Bouy et al. 2008; Sicilia-Aguilar et al. 2008; Riaz & Gizis 2008; Furlan et al. 2008; Pascucci et al. 2009; Olofsson et al. 2009; Riaz 2009; Riaz et al. 2009; McClure et al. 2010; Manoj et al. 2011; Furlan et al. 2011; Adame et al. 2011; Rilinger & Espaillat 2021).

However, the published sample of field dwarfs observed with the *Spitzer* IRS comprises only 60 per cent of all field \geq M5 dwarfs with IRS observations, based on comparisons of existing compilations of ultracool dwarfs (Section 2.1) with the *Spitzer* Heritage Archive (SHA)¹. In preparation for upcoming observations with the *James Webb Space Telescope*, we have uniformly reprocessed and analysed all *Spitzer* IRS observations of field ultracool dwarfs.

Herein we present all 113 field M5–T9 dwarfs that have detectable signal in their *Spitzer* IRS low-resolution spectroscopic observations. All IRS observations were obtained during the *Spitzer* cryogenic mission, which ended in 2009, before the discovery of the first Y dwarfs

* E-mail: gsuarez@uwo.ca

¹ <https://sha.ipac.caltech.edu/applications/Spitzer/SHA/>

(Cushing et al. 2011). None of the observed late-T dwarfs have since been re-classified as Y dwarfs. Hence, the presented compendium includes all field $\geq M5$ dwarfs with low-resolution *Spitzer* IRS observations. A subsequent publication will focus on young ultracool dwarfs with IRS spectra. In Section 2 we describe the observations and explain our updated procedure to extract the spectra. In Section 3 we analyse the strengths of the three main molecular species (H_2O , CH_4 , and NH_3) and of 8–11 μm silicate absorption to infer dependencies on spectral type, near-infrared colours, photometric variability, or binarity. We summarise our work and conclude in Section 4.

2 SAMPLE AND DATA REDUCTION

2.1 The *Spitzer* IRS Sample of Field M5–T9 Dwarfs

To search for spectroscopic observations of ultracool dwarfs obtained with the *Spitzer* IRS, we queried the SHA on a comprehensive list of field late-M, L and T dwarfs. The list is based on the compilation by W. Best and collaborators (The UltracoolSheet² as of 2021 March 7), which contains about 3000 spectroscopically confirmed objects, mainly L and T brown dwarfs in the solar neighbourhood ($\lesssim 100$ pc). The list was complemented with spectroscopically confirmed M5–M9 dwarfs from the compilation by J. Gagne³, that contains over 8500 objects with such spectral types, most of them (about 60 per cent) M6 dwarfs. The final compiled catalogue has more than 11000 M5–M9, L and T dwarfs, the vast majority of them field objects.

We retrieved IRS short-low (SL) module spectroscopic observations for a total of 156 M5–T9 dwarfs from the compiled catalogue. We used a 60'' search radius and verified the matches by comparing the object names and by checking the sky coverage map in the SHA. Most observations were obtained in the standard staring mode. Four dwarfs (2MASS J00361617+1821104, 2MASS J02550357–4700509, 2MASS J05591914–1404488, and ϵ Ind B) were observed in both staring mode and mapping mode, and two targets (2MASS J01075242+0041563 and 2MASS J21392676+0220226) were observed only in mapping mode. The vast majority of the observations include both SL orders (SL1 and SL2); only 12 targets lack SL2 module spectra. Thirty-one of the sources with IRS SL observations were also observed with the long-low (LL) spectroscopic module, 29 of which in both orders (LL1 and LL2). The SL and LL modules cover 5.2–14.8 μm and 13.9–38 μm , respectively, at $R \approx 90$ in order 2 of both modules.

Thirteen of the M5–T9 dwarfs with low-resolution IRS data (2MASS names; J00361617+1821104, J01365662+0933473, J01390120–1757026, J02550357–4700509, J04234858–0414035, J05591914–1404488, J08294949+2646348, J12255432–2739466, J12545393–0122474, J14563831–2809473, J19165762+0509021, J22041052–5646577, and J22383372–1517573) were also observed at high resolution with the IRS, six of which were published in Mainzer et al. (2007). However, there are no additional $\geq M5$ dwarfs with only high-resolution observations. In this work we present only the low-resolution IRS data.

Of the 156 M5–T9 dwarfs with *Spitzer*/IRS SL observations in our compiled catalogue, 121 are field objects and 35 are known members of young ($\lesssim 10$ Myr) stellar associations, namely Chamaeleon I, Lupus, Ophiuchus, Taurus, TW Hydra, and Upper Scorpius. Our present catalogue is thus very incomplete to IRS observations of $\geq M5$ dwarfs in such young stellar associations, of which we found

166 in the published literature (Section 1). In the present paper we focus on the field dwarfs, and defer the discussion of $\lesssim 10$ Myr old $\geq M5$ dwarfs to a follow-up paper. We note that while the vast majority of field dwarfs in our sample are old ($\gtrsim 1$ Gyr) objects, there are also some younger dwarfs. One set of examples includes objects that exhibit spectroscopic signatures of youth, such as: 0501–0010 and 1022+5825 (with very low and intermediate surface gravity, respectively; Cruz et al. 2009), the ≈ 300 Myr old dwarf HN Peg B (a.k.a., 2144+1446; Luhman et al. 2007a; Suárez et al. 2021), and the 40–400 Myr old dwarf 0758+3247 (Stephens et al. 2009). Others include objects that are kinematic members of nearby young moving groups, for instance: 0355+1133 and 1425–3650 (AB Doradus, ~ 100 Myr; Liu et al. 2013; Gagné et al. 2015), and 0136+0933 and 2139+0220 (Carina-Near, ~ 200 Myr; Gagné et al. 2017; Zhang et al. 2021). At such moderately young (few tens to hundreds of Myr) ages, these dwarfs are not expected to have mid-infrared excesses caused by circumstellar disks (e.g.; Calvet et al. 2005; Briceño et al. 2005; Downes et al. 2014). We have visually verified this in their IRS spectra (Figure 1–3). Therefore, we include both moderately young (few tens to hundreds of Myr) and old ($\gtrsim 1$ Gyr) field dwarfs in the following analysis and, for simplicity, collectively refer to them as ‘field’ dwarfs.

As we detail in Section 2.3, 113 of the 121 field $\geq M5$ dwarfs targeted with the IRS have usable spectra. Tables 1 and 2 list, respectively, select parameters (name, coordinates, discovery paper, spectral type, binarity, and variability) and the observing log (*Spitzer* AOR key, program ID and PI, spectroscopic module, exposure time, and observation date) of the 113 field dwarfs for which we present IRS low-resolution spectra. Hereafter we abbreviate the names of the targets as hhmm±ddmm, where the suffix is the right ascension (hours and minutes) and declination (degrees and minutes) at the J2000.0 equinox. We list optical and infrared spectral types (when available) of the objects, and prioritise optical spectral types for M and L dwarfs and infrared types for T dwarfs. Table 3 lists the 8 field $\geq M5$ dwarfs that were targeted with the IRS, but for which the data did not yield good extractions. These spectra have S/N~0 because either the exposure times were too short or the targets were off the slit.

2.2 Improved Reduction of the *Spitzer* IRS SL and LL Observations

We downloaded from the SHA all basic calibrated data (BCD)—also known as Level 1 products—of the targets in the input list with IRS low-resolution observations. The BCD are produced by the IRS pipeline after ramp fitting, dark subtraction, droop correction, linearity correction, flat fielding, and wavelength calibration. We further reduced the data by removing bad pixels (outliers and rogues) from the 2D spectral images using the IRS CLEAN tool⁴ with the appropriate IRS campaign mask and with different noise_floor and aggressive parameters (ranging between 0.1 and 0.5, and 1 and 2, respectively) for each target to remove as many bad pixels as possible without affecting the spectrum trace. We combined the 2D spectral images taken at the same nod position (for staring mode data) or map position (for mapping mode data) using the coadd script⁵ provided by the Spitzer Science Center (SSC). We then removed the

² <https://doi.org/10.5281/zenodo.4570814>

³ <https://jgagneastro.com/list-of-m6-m9-dwarfs/>

background of the combined 2D spectral images in staring mode by pairwise subtracting them. Any residual background was further removed by subtracting from each image row (i.e., perpendicular to the trace) the median flux of that row after excluding both nod traces. To remove background from the 2D spectral images obtained in mapping mode, we subtracted a median-combined image with the target off the slit from a median-combined image with the target in the slit. Any residual background was further removed as for the staring mode data.

Before extracting the spectra, we again ran IRSCLEAN to remove residual bad pixels marked by hand on the background-subtracted images. The spectroscopic extraction was performed with the *Spitzer* IRS Custom Extraction (SPICE) software⁶ developed by the SSC. We used the default trace widths (4 pixels at 6 μm , 8 pixels at 12 μm , 4.25 pixels at 16 μm , and 7.172 pixels at 27 μm for the SL2, SL1, LL2, and LL1 spectroscopic modules) to obtain flux-calibrated spectra (in Jy). We evaluate the accuracy of this flux calibration in Section 2.4. Spectra obtained with the same module and in the same order were averaged. When assembling observations in multiple orders or modules, we used SL2 spectra for $5.2 \leq \lambda (\mu\text{m}) \leq 7.5$ and SL1 for longer wavelengths in the SL module (up to 14.1 μm), and LL2 for $14.1 < \lambda (\mu\text{m}) \leq 20.5$ and LL1 for $20.5 < \lambda (\mu\text{m}) \leq 38$ in the LL module. Thus, for targets observed in both SL and LL modules, we present a single 5.2–38 μm spectrum. Any offsets between the flux densities among the modules were removed by scaling the LL spectrum to the SL spectrum in the 13.9–14.8 μm overlap region.

The uncertainties of the spectra were obtained in three steps. First, when combining the BCD, an uncertainty 2D image (*c2unc*) was created considering the scatter of the individual frames. Then, in the background subtraction process new uncertainty frames (*bkunc*) were created by adding in quadrature the *c2unc* uncertainties of each pair of 2D images. Finally, the *bkunc* uncertainties of the pixels at each wavelength resolution element in the extraction trace widths were added in quadrature to obtain the uncertainties of the extracted spectra.

2.3 Reduced Low-resolution IRS Spectra for All 113 Field M5–T9 Dwarfs in the SHA

We successfully extracted 113 spectra of the 121 field M5–T9 dwarfs observed with the IRS. Twelve of these 113 spectra belong to M5–M9 dwarfs, 69 to L-type dwarfs, and 32 to T-type dwarfs. In Figures 1, 2, and 3 we show the 5.2–14.2 μm IRS spectra (7.5–14.2 μm for the five latest T dwarfs) of the objects with SL module observations. Eighteen of the 113 spectra have both SL and LL data. Figure 4 shows the 5.2–38 μm IRS spectra (5.2–20.5 μm for 0024–0158 and 1225–2739) of these 18 targets. In Table 2 we list all 113 dwarfs together with the signal-to-noise ratio (S/N) at 6 and 12 μm of the IRS spectra. The median S/N is ≈ 20 at 6 μm and ≈ 10 at 12 μm .

Our final sample contains *Spitzer* IRS spectra of 36 M7–T9 dwarfs that are discussed for the first time. The remaining 77 M5–T9 dwarfs with IRS low-resolution spectra have already been discussed in preceding studies (Roellig et al. 2004; Cushing et al. 2006; Saumon et al. 2007;Looper et al. 2008; Burgasser et al. 2008c; Leggett et al. 2009; Stephens et al. 2009; Kirkpatrick et al. 2010; Leggett et al. 2010b; Filippazzo et al. 2015; Suárez et al. 2021), as referenced in Table 2. However, spectra for 32 of these 77 previously analysed

objects have not been shown or made publicly available. Therefore, our work makes IRS spectra for 68 ultracool dwarfs, over half of the field ultracool IRS sample, available for the first time.

2.4 Accuracy of the IRS Flux Calibration

We evaluated the accuracy of the automatic flux calibration of the IRS spectra by comparing IRAC channel 4 (8.0 μm , [8.0]) and WISE W3 photometry of the targets with synthetic photometry from the IRS spectra. For the [8.0]-band comparisons we considered sources having both SL module orders (SL1 and SL2) to get full spectral coverage of the [8.0] pass band (6.30–9.59 μm). On the other hand, to cover the entire W3 pass band (7.44–17.26 μm), we require IRS spectra with both SL and LL modules (at least LL2 order). From our sample of 113 IRS spectra, 108 meet the first criterion and 18 meet the second criterion. We obtained the synthetic flux F_{syn} over the band pass (λ_A, λ_B) by convolving the filter response S_{λ} with the synthetic spectrum F_{λ} :

$$F_{\text{syn}} = \frac{\int_{\lambda_A}^{\lambda_B} F_{\lambda} S_{\lambda} d\lambda}{\int_{\lambda_A}^{\lambda_B} S_{\lambda} d\lambda} \quad (1)$$

The synthetic fluxes were converted to synthetic magnitudes m_{syn} to be compared with the observed magnitudes m_{obs} listed in Table 4. For 67 of the 70 dwarfs with observed [8.0] magnitudes we calculated the corresponding [8.0]-band synthetic magnitudes, as they have full spectral coverage of the [8.0] filter pass band. Fourteen of these also had IRS LL2 coverage that enabled comparisons of their synthetic and observed W3 magnitudes. Four additional dwarfs without observed [8.0] magnitudes had WISE W3 magnitudes, and also sufficient spectral coverage to calculate the corresponding synthetic W3 magnitudes. Thus, a total of 71 M5.5–T8 dwarfs had [8.0] or W3 photometry and sufficient IRS spectral coverage to compare measured vs. synthetic fluxes.

For the comparison we excluded three sources with differences between measured and synthetic magnitudes that were larger than 5 times the standard error of the mean (SEM; σ/\sqrt{N} , where σ is the data scatter and N is the sample size). Two are outliers (0000+2554 and 0501–0010) in the [8.0] photometric comparison and one (2238–1517) at W3. (In Section 2.5 we further improve the flux calibration of these and other discrepant objects). After outlier removal, the average and SEM of the [8.0] and W3 residuals are mutually consistent: -0.071 ± 0.015 mag and -0.039 ± 0.034 mag, respectively. When considering both band passes together, the difference between the observed and synthetic magnitudes is -0.064 ± 0.014 mag. We added this -0.064 mag average offset to our synthetic magnitudes reported in Table 4 and applied the corresponding scaling (by a factor of 1.06) to all IRS spectra presented in this study. In Figure 5 we show the residuals between observations and synthetic photometry after applying the flux calibration correction.

2.5 Improvement of the IRS Flux Calibration for Individual Targets

We evaluated in Section 2.4 the overall IRS flux calibration accuracy of field M5–T9 dwarfs with full IRS wavelength coverage of either the IRAC [8.0] or the WISE W3 pass bands. However, we could not verify the automatic flux calibration for about 40 per cent of our 113 objects because they lack SL2 and/or LL2 observations, and so do not fully cover the [8.0] or W3 filter pass bands. In order to provide the community with a flux-calibrated mid-infrared spectroscopic sample

⁶ <https://irsa.ipac.caltech.edu/data/SPITZER/docs/dataanalysis/tools/spice/>

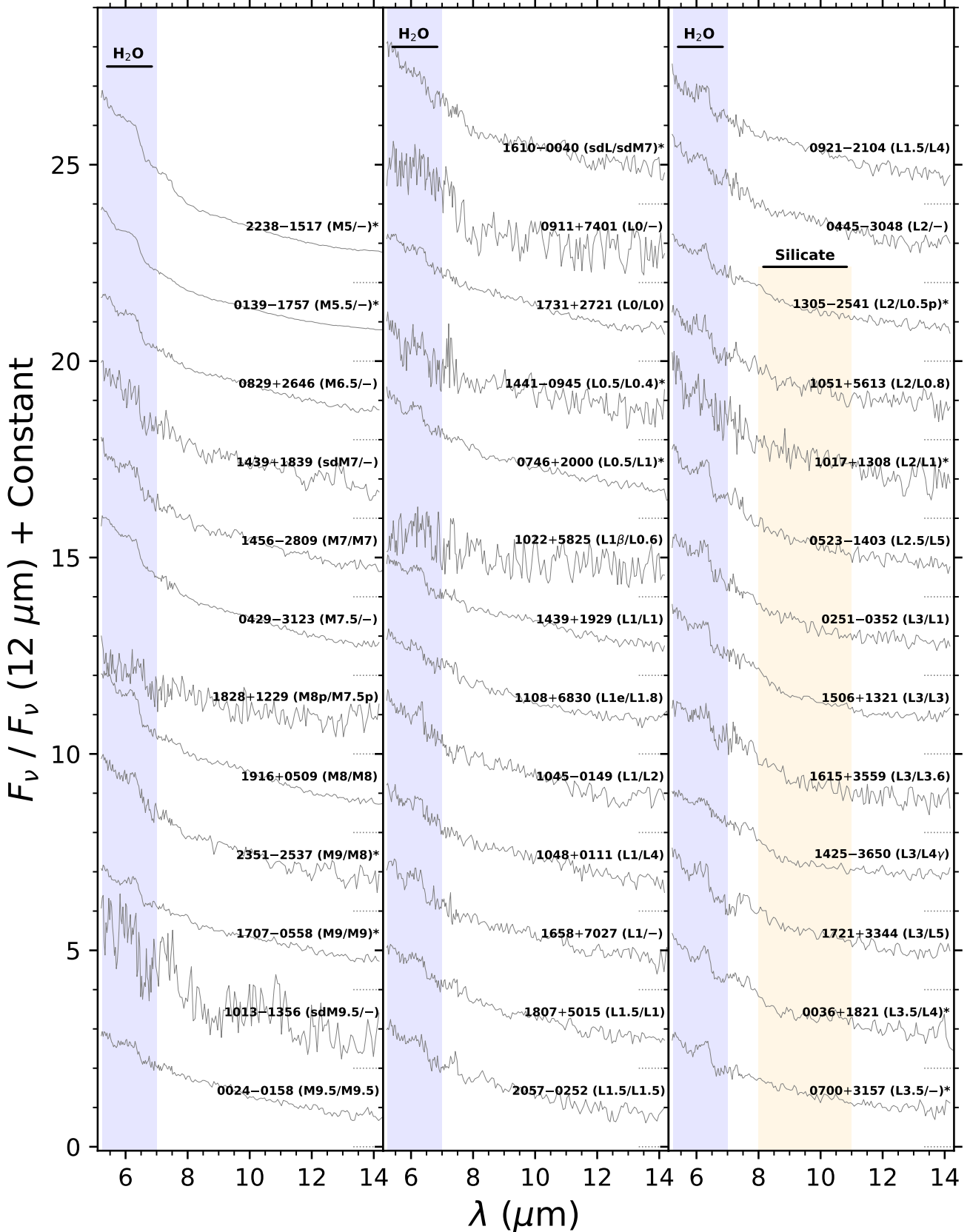


Figure 1. *Spitzer* IRS 5.2–14.2 μm spectra of 12 M5–M9 dwarfs (left panel) and 26 L0–L3 dwarfs (middle and right panels). The spectra were normalised to unity using the median flux at 12 μm in a 0.6 μm window and offset by constants (dotted lines). Binary sources are indicated with asterisks (Table 1). The optical and near-infrared spectral types (when available) of the dwarfs are indicated in the labels. The absorption regions for water and silicates are shaded. (The spectra shown in this figure are available in the online journal.)

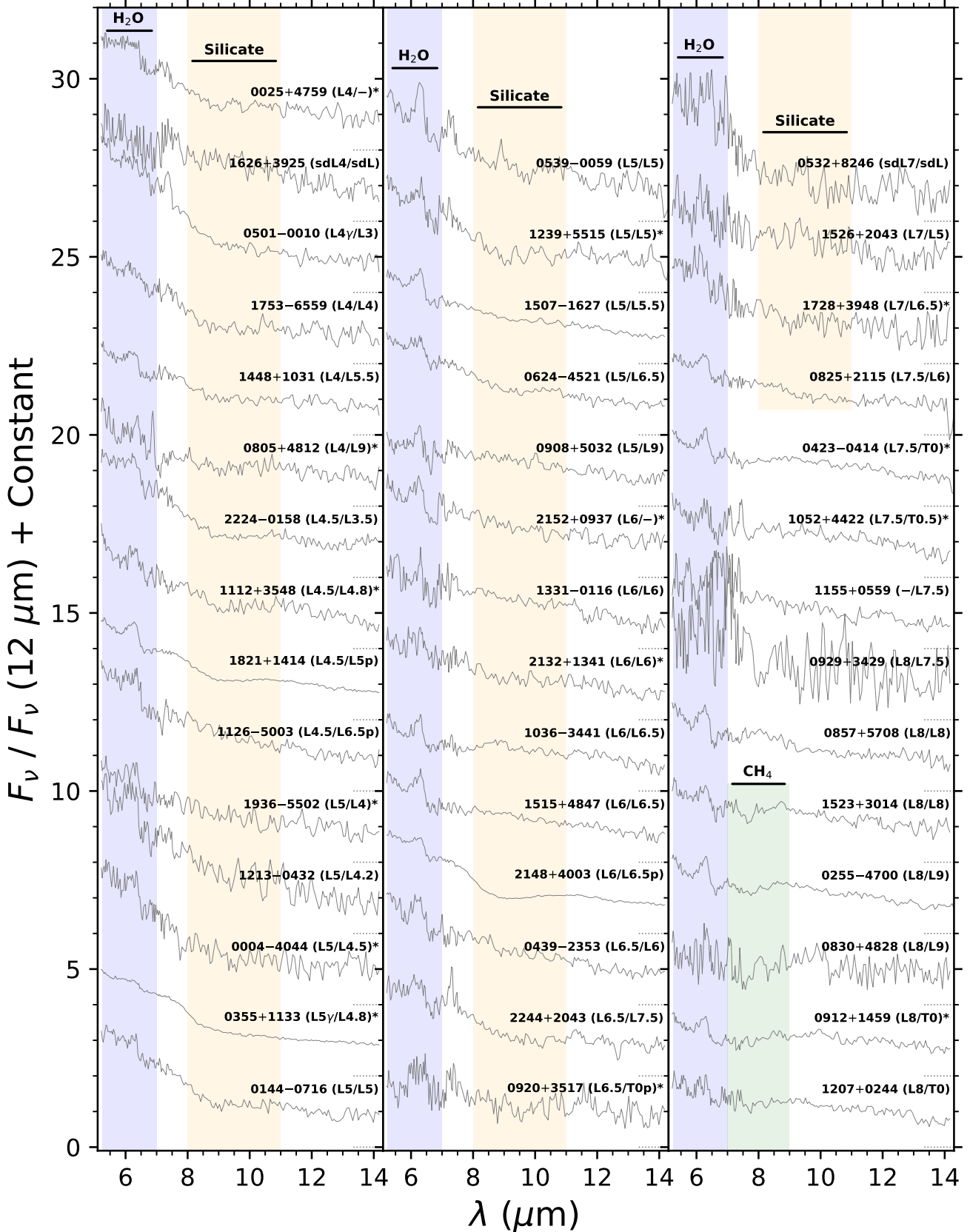


Figure 2. *Spitzer* IRS 5.2–14.2 μm spectra of 43 L4–L8 dwarfs. The spectra were normalised to unity using the median flux at 12 μm in a 0.6 μm window and offset by constants (dotted lines). Binary sources are indicated with asterisks (Table 1). The optical and near-infrared spectral types (when available) are indicated in the labels. The absorption regions for water, methane, and silicates are shaded. (The spectra shown in this figure are available in the online journal.)

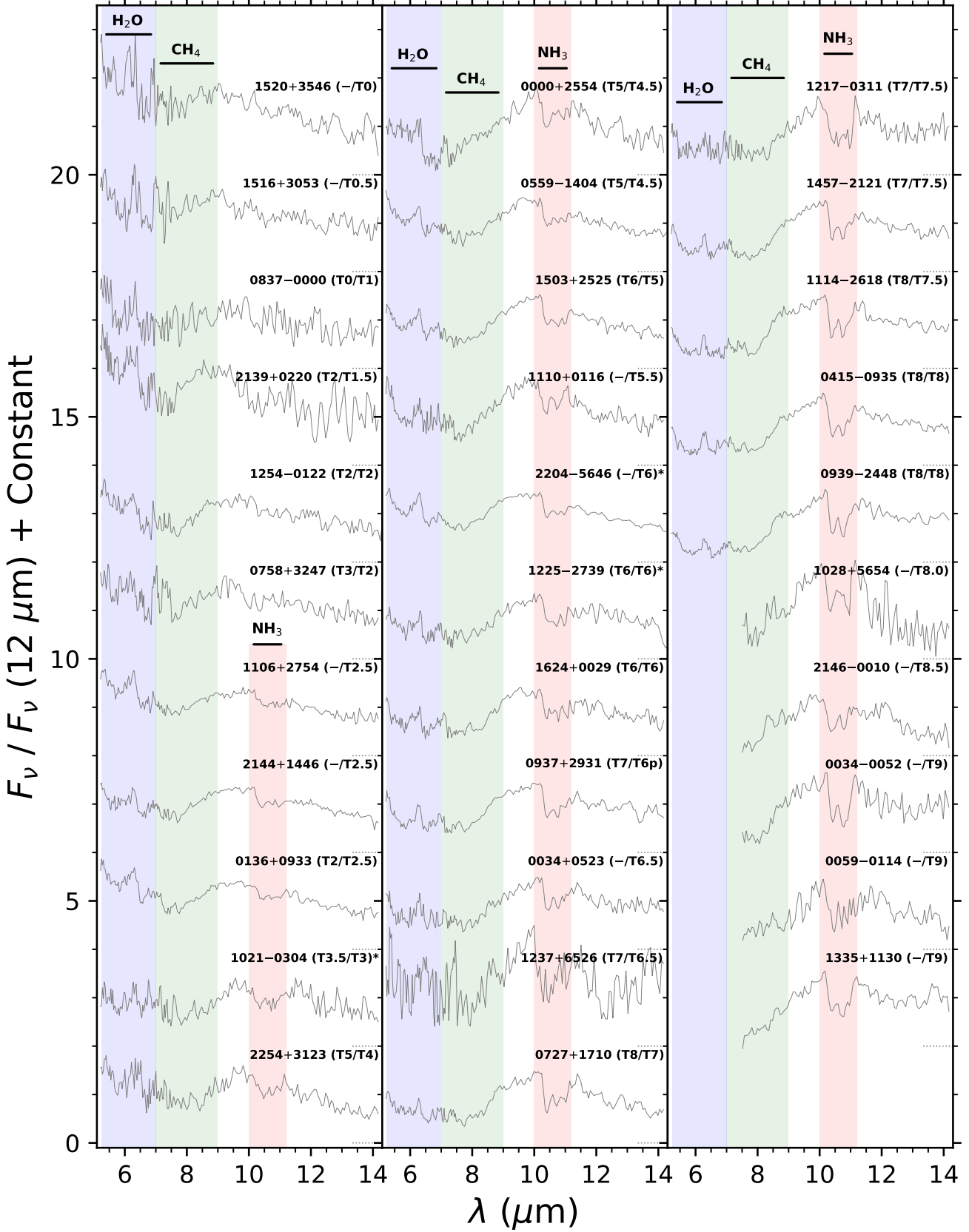


Figure 3. *Spitzer* IRS 5.2–14.2 μm spectra of 27 T0–T8 dwarfs and 7.5–14.2 μm IRS spectra of 5 T8–T9 dwarfs. The spectra were normalised to unity using the median flux at 12 μm in a 0.6 μm window and offset by constants (dotted lines). Binary sources are indicated with asterisks (Table 1). The optical and near-infrared spectral types (when available) are indicated in the labels. The absorption regions for water, methane, and ammonia are shaded.

(The spectra shown in this figure are available in the online journal.)

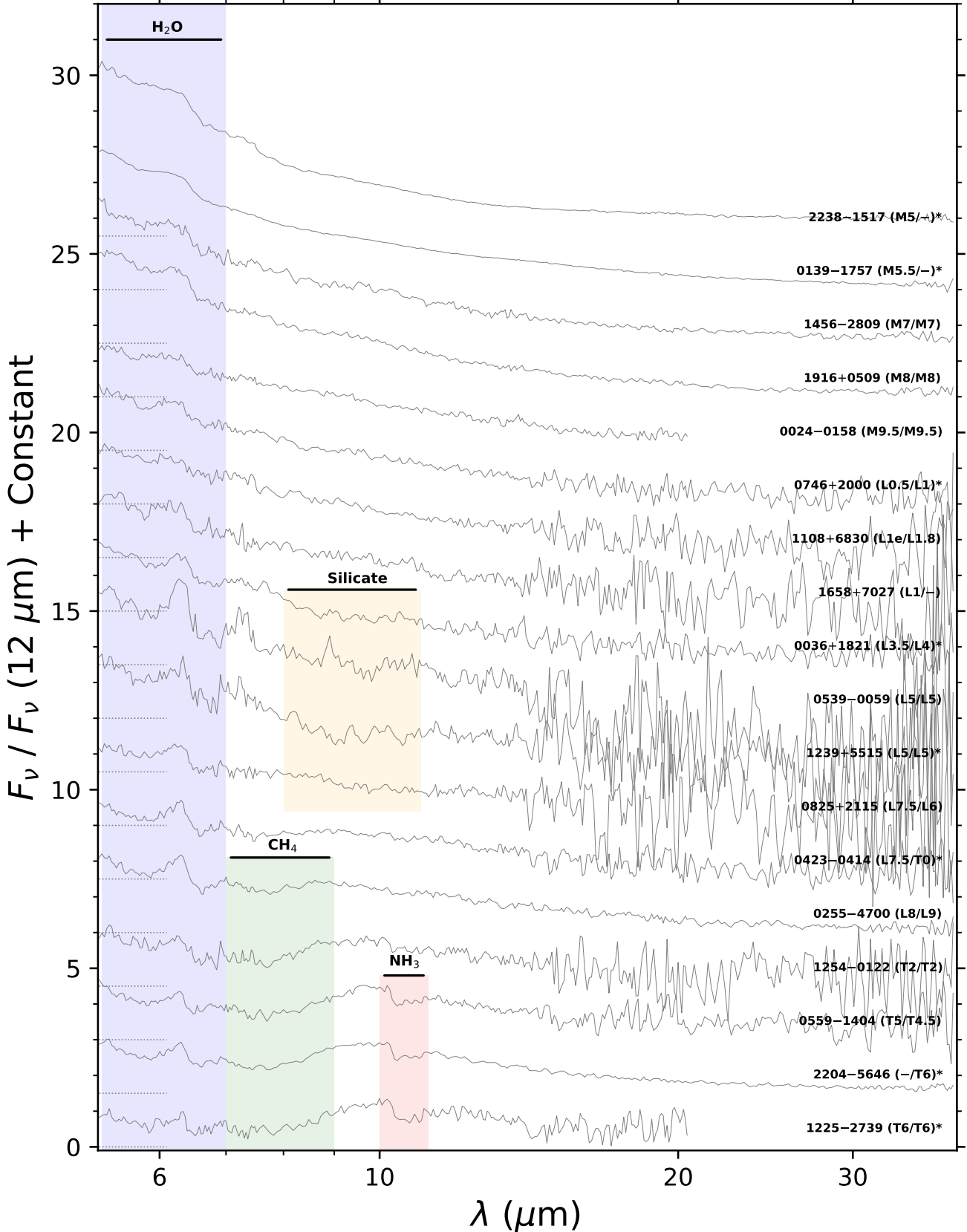


Figure 4. *Spitzer* IRS 5.2–38 μm spectra of 18 M5–T6 dwarfs (5.2–20.5 μm for 0024–0158 and 1225–2739). The spectra were normalised to unity using the median flux at 12 μm in a 0.6 μm window and offset by constants (dotted lines). Binary sources are indicated with asterisks (Table 1). The optical and near-infrared spectral types (when available) are indicated in the labels. The absorption regions for water, methane, silicates, and ammonia are shaded. (The spectra shown in this figure are available in the online journal.)

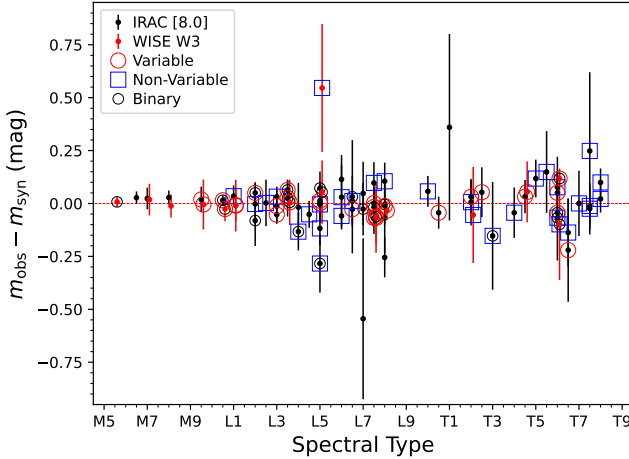


Figure 5. Residuals between observed and synthetic magnitudes using the IRAC [8.0] (black points) and WISE W3 (red points) pass bands as a function of spectral type after correcting by the average offset of -0.064 ± 0.014 mag along the whole spectral type range (see Section 2.4). The synthetic photometry was obtained from the IRS spectra presented in this study. The corrected 8 and 12 μm IRS fluxes scatter with an RMS of 14 per cent. The W3 comparison points are shifted slightly to the right for clarity. The red circles, blue squares, and black circles indicate variable, non-variable, and binary sources (Table 1), respectively.

of ultra-cool dwarfs, we further assess the flux calibration of the IRS spectra as follows.

The five latest (T8–T9) dwarfs in our sample were not observed in SL2 mode, and so lack spectra shortward of 7.50 μm . To complement their wavelength coverage so that it fully encompasses the [8.0] 6.30–9.59 μm filter pass band, we extended the spectra from 7.50 μm to 6.30 μm using the average IRS SL2 spectrum of the T8 dwarfs 0415–0935 and 0939–2448 (Figure 3).

A larger number (95) of our 113 targets were not observed in LL2 mode (Table 2), and so lack spectra longward of 14.2 μm . To complement their wavelength coverage so that it fully encompasses the W3 7.44–17.26 μm filter pass band, we extended the spectra from 14.20 μm to 17.26 μm with the LL2 spectrum of an object most similar in spectral type (Figure 4). When two templates with the same spectral type and similar S/N are available, we used the average IRS spectrum. The templates cover spectral types M5–T6 in steps of no more than 3 subtypes. Thus, each extension was done using a template within 1.5 subtypes from the spectral type of the target, except for the latest dwarfs, for which the template has a spectral type difference of up to 3 subtypes. However, as the IRS LL M5–T9 spectra appear featureless in the extension region (Figure 4), the IRS spectra at these wavelengths have essentially the same Rayleigh-Jeans behaviour.

We used Equation 1 to obtain synthetic [8.0] and W3 photometry from all extended IRS spectra scaled up by the overall factor of 1.06 determined in Section 2.4. The resulting synthetic magnitudes were compared to the observed IRAC [8.0] and WISE W3 magnitudes (Table 4). If the synthetic and the observed magnitudes were more than 3σ or 0.5 mag discrepant, we scaled the IRS spectrum to the observed photometry. When both [8.0] and W3 observed magnitudes were available for the same object, the IRS flux of the object was corrected only if the criterion was met in both comparisons.

We applied this additional calibration of the IRS fluxes to a total of 13 of our 113 M5–T9 dwarfs, including the three outliers mentioned

in Section 2.4 (0000+2554, 0501–0010, and 2238–1517) and 10 additional dwarfs (0532+8246, 0830+4828, 0911+7401, 1022+5825, 1106+2754, 1213–0432, 1441–0945, 1821+1414, 2139+0220, and 2148+4003). Two of these 13 objects were identified from the [8.0] magnitude comparison, nine from the W3 comparison, and one from both comparisons.

The likely reason for the highly discrepant IRS vs. [8.0] and/or W3 fluxes for these 13 objects is inadequate positioning on the IRS slit because of inaccurate knowledge of the objects' precise coordinates. The M5–T9 dwarfs in the sample are generally too faint for on-target acquisition with the blue (15 μm) or red (22 μm) IRS peak-up imaging (PUI) camera, and so would have required offset acquisition with respect to a nearby $V < 10$ mag target using the 505–595 nm Pointing Calibration and Reference Sensor (PCRS) on Spitzer (Houck et al. 2004). Doing so requires accurate knowledge of the proper motion of the science target, which for our M5–T9 dwarfs can be significant ($\gtrsim 200$ mas yr^{-1}). However, during the pre-WISE and pre-Gaia 2004–2009 epoch of Spitzer IRS observations, the proper motions would not have been known to sufficient accuracy to centre the targets on the Spitzer IRS slit (3.7'' width for SL1). Consequently, the lost flux would not have been accounted for in the SSC pipeline extraction, resulting in a significant discrepancy between the IRS fluxes and the [8.0] or W3 band photometry. We believe this to be the case for the most discrepant IRS spectra, given that a further eight of the 121 field M5–T9 dwarfs targeted with IRS did not yield any detectable signal at all (Table 3): as would be expected from even poorer alignment.

We used the fully flux-calibrated IRS spectra of the 113 field M5–T9 dwarfs to analyse their main mid-infrared spectral features in the next section.

3 SPECTRAL FEATURES

3.1 Molecules: Water, Methane, and Ammonia

We measured the depths of the H₂O, CH₄, and NH₃ absorption at 6.25 μm , 7.65 μm , and 10.5 μm , respectively, considering the spectral index definitions in Cushing et al. (2006). We modified the Cushing et al. (2006) definition for the methane index to sample the region of strongest absorption, at the 7.65 μm methane band head, instead of at 8.5 μm :

$$\text{H}_2\text{O Index} = \frac{F_{6.25}}{0.562F_{5.80} + 0.474F_{6.75}}, \quad (2)$$

$$\text{CH}_4 \text{ Index} = \frac{F_{10.0}}{F_{7.65}}, \quad (3)$$

$$\text{NH}_3 \text{ Index} = \frac{F_{10.0}}{F_{10.8}}. \quad (4)$$

F_λ above is the mean flux density around the specified wavelength (in μm) in a window of 0.3 μm for the water index and 0.6 μm for both the methane and the ammonia indices. For an illustration of these index definitions we refer the reader to Figure 6 in Cushing et al. (2006).

We computed the above three spectral indices for most dwarfs in our sample. The water index for the five latest T dwarfs could not be computed because, as they lack $\lambda \leq 7.5 \mu\text{m}$ IRS SL2 data (Figure 3; Table 2), there is no full spectral coverage of the absorption. In Table 5 we list the index measurements of the main molecular features (H₂O, CH₄, and NH₃) in the IRS spectra of 113 field M5–T9 dwarfs. The index uncertainties were obtained from the uncertainties in the mean flux densities of both the absorption and the continuum. In the first three panels of Figure 6 we show the index values as a

function of spectral type. The median index values in spectral type bins of two subtypes (to average down statistical scatter) are connected with a dashed black line for each absorber. We highlighted with a different colour (red points) the targets in the Cushing et al. (2006) sample to distinguish them from the new dwarfs in our sample (black points). We increased the sample of M5–T9 dwarfs with IRS molecular absorption measurements from 38 to 113 objects (a ≈200 per cent increase). We notice the significant addition of dwarfs particularly at early-T types.

We see from Figure 6 that H₂O absorption overall strengthens with spectral type from M5 to T9, even if it remains roughly constant within a large scatter between L8–T7. The onset of CH₄ absorption at the resolution and S/N of the IRS data is at about spectral type L8, and rapidly strengthens toward later spectral types. The actual spectral type of CH₄ onset is subject to ambiguity in the optical vs. near-infrared spectral classification or binarity of L/T-transition dwarfs. In particular, the unresolved binary 0423–0414, which has a composite spectral type of L7.5/T0 (optical/near-infrared) and for which we adopt a spectral type of L7.5 in our analysis, already exhibits CH₄ absorption at 7.65 μm (Figures 2 and 4). The individual components of 0423–0414 have spectral types of L6 ± 1 and T2 ± 1 (Burgasser et al. 2005b). Hence, the CH₄ absorption is likely caused by the T2 component.

We also see in Figure 6 that NH₃ absorption becomes detectable first in 2139+0220 at (near-infrared) spectral type of T1.5 and is consistently present in ≥T2.5 dwarfs (Figure 3). Ammonia strengths increase marginally toward cooler temperatures.

Overall, our assessment of mid-infrared molecular absorbers is consistent with the findings in Cushing et al. (2006), who report that both CH₄ and NH₃ set in around the L/T transition in *Spitzer* IRS spectra. Our uniform analysis of the more comprehensive sample increases the robustness of these results.

Known binaries and variables scatter around the median index values of the water, methane, and ammonia absorption bands (top three panels of Figure 6). That is, neither the composite spectroscopic signature of an unresolved binary nor the presence of photometric variability discernibly bias the overall trends of molecular absorption strengths in the low-resolution IRS data. However, as we discuss in Section 3.2.3, we find a weak correspondence between the presence of silicate absorption and known photometric variability.

3.2 Dust: Silicates

In substellar atmospheres the silicate compound that is expected to condense at highest temperatures is forsterite (Mg₂SiO₄), at $T \approx 1700$ K (Lodders 2002, at $P = 1$ bar). The condensation temperature increases or decreases, respectively, by ≈100 K for $P = 10$ bar or 0.1 bar. At ≈50–100 K cooler temperatures, the SiO present in (equilibrium) atmospheres and the forsterite react to form enstatite (MgSiO₃; Lodders 2002). The 1600–1700 K condensation temperatures of forsterite and enstatite correspond to mid-L spectral types (e.g.; Filippazzo et al. 2015).

Silicate molecules are known to have prominent broad spectroscopic signatures in the 8–12 μm range (e.g., Draine & Lee 1984; Hanner et al. 1994). Previous analyses of *Spitzer* IRS spectra have already noted the presence of a 9–11 μm plateau in several L dwarfs. Cushing et al. (2006) found that a combination of enstatite and forsterite condensates with small particle sizes ($\lesssim 2$ μm radii) is able to reproduce the 9–11 μm flattening in the IRS spectrum of the L4.5 dwarf 2224–0158 (Figure 2). They observed a similar plateau in the IRS spectrum of 0036+1821 (L3.5) and a similar but weaker feature in 1507–1627 (L5). Looper et al. (2008) also identified this feature in

the IRS spectra of 1821+1414 and 2148+4003 (L4.5 and L6; Figure 2) and attributed it to silicate absorption. Helling et al. (2006) posit that the 9–11 μm feature could arise from quartz (SiO₂) grains, and note that it is absent in equilibrium models. They suggest that the detection of this feature could provide evidence for non-equilibrium dust formation in brown dwarf atmospheres. Accordingly, Burningham et al. (2021) reported that a combination of enstatite and quartz condensates with iron clouds at different pressure layers reproduces well the 9 to 11 μm flattening in the IRS spectrum of 2224–0158.

In our full IRS sample, we observe that a broad absorption feature is present in some L dwarfs between 8–11 μm. We refer to this feature as “silicate” absorption, which we take to encompass the signatures of enstatite, forsterite, or quartz grains. Our ensemble analysis of all low-resolution *Spitzer* IRS spectra shows that silicate absorption sets in as early as the L2 spectral type and is discernible through the end of the L dwarf sequence.

3.2.1 Silicate Absorption Strengths: Emergence and Sedimentation of Silicate Condensates in L Dwarfs

We assessed the absorption strength over 8–11 μm in all IRS spectra of M5–T8 dwarfs. We defined the silicate index as the ratio of the interpolated continuum flux ($C_{9.0}$) at 9 μm to the average flux ($F_{9.0}$) in a window of 0.6 μm centred at 9 μm. The interpolated continuum flux was obtained considering the best linear fit to the fluxes at 7.5 and 11.5 μm in a 0.6 μm window, as shown in Figure 7. Thus, the index is given by

$$\text{Silicate Index} = \frac{C_{9.0}}{F_{9.0}} \quad (5)$$

As for the water index in Equation (2), we did not compute the silicate index for the five latest T dwarfs (Table 1) because they do not have full spectral coverage in the region defined to measure the continuum of the feature. The silicate index uncertainties were obtained from the uncertainties in the mean flux density of the absorption and in the continuum fit. We list the silicate index measurements in Table 5, and we present them as a function of spectral type in the bottom panel of Figure 6.

The trend in silicate index measurements over M5–T8 dwarfs, traced by the dashed curve in the bottom panel of Figure 6, shows a clear upward deviation in the L dwarfs. The above-trend silicate index values of L dwarfs indicate prevalent silicate absorption. The feature is discernible in the spectra of objects as early as spectral type L2 and as late as L8, and peaks in strength in L4–L6 dwarfs. At the same time, at all L subtypes—even at mid-L—there are objects that do not show any discernible silicate absorption. The diversity in silicate absorption strengths within a narrow spectral type range points to active sedimentation of different-particle size silicate condensates to deeper atmospheric layers and higher pressures, where they fall below the $\lesssim 1$ bar 8–11 μm photosphere (Cushing et al. 2006; Karalidi et al. 2021).

The temperatures corresponding to the spectral types for the onset (L2) and disappearance (L8) of the silicate absorption in the IRS spectra are 1960 K and 1340 K, respectively, while the spectral type range where the feature is on average the strongest (L4–L6) corresponds to temperatures between 1690 K and 1480 K (Filippazzo et al. 2015). The polynomial relationship between effective temperature and spectral type in Filippazzo et al. (2015, Table 10) has an r.m.s. scatter of 113 K. A ≈2000 K onset temperature for silicate absorption is consistent with the recent finding that silicate condensation must begin between equilibrium temperatures $1950 \text{ K} < T_{\text{eq}} <$

2450 K in exoplanetary atmospheres (Lothringer et al. 2022). Specifically, Lothringer et al. (2022) detect the gas-phase SiO constituent of silicate molecules (MgSiO_3 , Mg_2SiO_4) in the UV transmission spectra of $T_{\text{eq}} = 2350$ K and $T_{\text{eq}} = 2450$ K transiting planets, but do not see it in the UV transmission spectrum of a cooler $T_{\text{eq}} = 1950$ K transiting planet. Our result confirms that at this cooler temperature SiO would already be bound in silicates.

It is possible that silicates may start condensing at slightly earlier spectral types and warmer temperatures. There are three M9.5–L1 ($2320 \text{ K} \geq T_{\text{eff}} \geq 2100 \text{ K}$) dwarfs (1013–1356, 0911+7401, and 1022+5825) with a high silicate index (>1.2). However, they also have large (≥ 20 per cent) silicate index uncertainties due to the low S/N (<5 at $12 \mu\text{m}$) of their IRS spectra, such that the detection of the feature is not significant. None of the $\leq \text{M9}$ ($T_{\text{eff}} \geq 2400$ K) dwarfs or $\geq \text{T0}$ ($T_{\text{eff}} \leq 1250$ K) dwarfs show any silicate absorption at the $\text{S/N} \lesssim 100$ and $R \approx 90$ resolution of most archival IRS spectra.

3.2.2 Positive Correlation between Silicate Absorption and Near-infrared Colour Excess

It is established that certain L dwarfs with prominent silicate absorption in their IRS spectra (1821+1414, 2148+4003, and 2224–0158) have redder colours than expected for their spectral types (Cushing et al. 2006, 2008;Looper et al. 2008).Looper et al. (2008) suggested that the redness of 1821+1414 and 2148+4003 is due to unusually dusty atmospheres caused by high metallicity or low surface gravity. If the colour peculiarities of L dwarfs at a given subtype are caused by condensate silicate clouds, a correlation between colours and the absorption strength of the Si-O feature could be expected (Burgasser et al. 2008a; Cushing et al. 2008;Looper et al. 2008). We investigate this correlation with our IRS spectra in the following.

We selected the dwarfs with the largest (>1.2) silicate index values—above the dotted line in the bottom panel of Figure 6—and with fractional errors <20 per cent. We visually verified in Figures 1 and 2 that the selected dwarfs indeed show a flux deficit between 8 and $11 \mu\text{m}$. The resulting sample of 21 dwarfs spans the L3–L7 spectral subtypes, and includes the four objects previously reported to exhibit strong silicate features (0036+1821 and 2224–0158 in Cushing et al. 2006, and 1821+1414 and 2148+4003 in Looper et al. 2008). Two other L dwarfs with previously reported weak silicate absorption, 0255–4700 (L8; Roellig et al. 2004) and 1507–1627 (L5; Cushing et al. 2006;Looper et al. 2008), were not selected because their silicate index values are below our threshold.

Figure 8 shows the IRS spectra of the 21 L3–L7 dwarfs selected to have strong silicate absorption. The optical and near-infrared spectral types (when available) of these dwarfs are in agreement within one subtype, except for 0920+3517. This object has an adopted (Section 2.1) optical spectral type L6.5 (Kirkpatrick et al. 2000), but its infrared classification is T0 (Burgasser et al. 2006b). It is in fact a known close binary with the individual components having near-infrared spectral types of L5.5 and L9 (Dupuy & Liu 2012). As the binary is not resolved in the *Spitzer* IRS beam, we are likely seeing the brighter L5.5 dwarf dominating the mid-infrared continuum.

In Figure 9 we compare the 2MASS near-infrared colours of the L3–L7 dwarfs with the strongest silicate absorption (marked with red data points) to the median 2MASS colours of all dwarfs in the Ultra-coolSheet catalogue (marked with grey data points), as a function of spectral type. We observe that the dwarfs with the strongest silicate absorption are preferentially redder in all near-infrared colour combinations, even if they lie within the 68 per cent central confidence interval (grey band) for most cases.

We further investigate this behaviour by comparing the silicate

index values of 37 of the 39 L3–L7 dwarfs with IRS spectra with their 2MASS near-infrared colour excesses. We define the colour excess of an object as the difference between its observed colour and the median colour for its spectral type (Figure 9). Working with colour excesses rather than just colours removes the dependence on spectral type and isolates the potential role of reddening by silicate dust. The two mid-L objects excluded from this analysis are the subdwarfs 0532+8246 (sdL7) and 1626+3925 (sdL4) because they have very blue 2MASS colours (Figure 9). (As the only L subdwarfs in our sample, these two objects are expected to have condensate-free atmospheres, so we are justified in excluding them from our analysis of silicate absorption strengths.) Figure 10 shows this comparison, and reveals a positive correlation between silicate absorption strength and 2MASS colour excess. That is, L3–L7 dwarfs that are redder than average exhibit a stronger silicate absorption, while bluer dwarfs have a weak or absent absorption. The Pearson correlation coefficients r are between 0.5 and 0.7 with p -values of <0.2 per cent: indicative of a moderate to strong correlation (Cohen 1988). We verified that similar but less significant ($0.4 \leq r \leq 0.5$) correlations hold for all L0–L8 dwarfs with IRS spectra (excluding the two L subdwarfs).

This result is consistent with the scenario where the near-infrared colour scatter (including peculiar colours) at a given L subtype is caused by differences in dust cloud thickness (Knapp et al. 2004; Burgasser et al. 2008a; Cushing et al. 2008;Looper et al. 2008). Specifically, L dwarfs in which the silicate condensate column extends into the <1 bar upper atmosphere, where it is detectable with *Spitzer* IRS, tend to on average have redder near-infrared colours.

3.2.3 Silicate Absorption vs. Photometric Variability: Variable mid-L Dwarfs Are Preferentially Silicate-rich Objects

Photospheric clouds are considered the leading mechanism for photometric variability in L and T dwarfs (e.g., Burgasser et al. 2002; Marley et al. 2010; Radigan et al. 2014; Miles-Páez et al. 2017b; Biller 2017, and references therein). Apai et al. (2013) further note that photometric variability in L and T dwarfs is associated with near-infrared colour excursions along a dust extinction track: consistent with varying cloud thickness if the clouds are composed of dust. It could thus be anticipated that if dust clouds are responsible for the observed photometric variability in L dwarfs, then the presence of silicate absorption could be related to observed variability.

Thirty-nine of the field M5–T9 dwarfs in the *Spitzer* IRS sample have been reported to be photometrically variable from previous $<5 \mu\text{m}$ observations (considering the compilation of L and T variables in Tannock et al. 2021 and complementing with additional references, as listed in Table 1). We can test whether L dwarfs displaying mid-infrared silicate absorption are also more likely to be known as variables. We focus specifically on the 37 L3–L7 dwarfs, among which we have the 21 objects with the strongest silicate absorption (Section 3.2.2; excluding the two L subdwarfs). Out of these 37 L3–L7 dwarfs, 27 have been monitored for variability, with 15 detected variables and 12 non-variables. For the remaining 10 we could not find literature references to variability monitoring. All variables are marked with red circles in Figures 6, 9, and 10, and known non-variables are marked with blue squares.

For clarity, we have extracted the variability information in a separate Figure 11. The left panel of Figure 11 is a simplified version of the bottom panel of Figure 6, that contains only the variability indications. Similarly, the right three panels of Figure 11 are simplified versions of the three panels in Figure 10.

Of the 15 variable L3–L7 dwarfs, 11 have above-average silicate absorption for their spectral types (dark dashed curve in the left panel

of Figure 11) and four are below average. If silicate absorption was independent of variability, the binomial probability of having 11 or more variables with above-average silicate strength is 5.9 per cent. Conversely, of the 12 known non-variable L3–L7 dwarfs, only four have above-average silicate strengths, and eight have weaker silicate. Again, the binomial probability of having at most four variables with above-average silicate occurring at random is 19.4 per cent. Neither of these probabilities are very low individually, but the joint occurrence of the phenomena is even less probable. These two distributions are not independent, because they jointly contribute to the calculation of the average silicate absorption strength. To properly assess the joint probability of randomly having at least 11 silicate-rich objects among the 15 variables, and at most 4 silicate-rich objects among the 12 non-variables, we performed a Monte Carlo simulation with 10^6 realisations of a sample of 37 L3–L7 dwarfs (of which 15 are variables, 12 are non-variables, and 10 are with an unknown variability status). In only 1.2 per cent of cases did a similar or more extreme distribution occur at random. Hence, our analysis shows that silicate absorption and photometric variability are co-dependent with 98.8 per cent significance.

The comparison between silicate absorption strength and near-infrared colour excess is less indicative of a correlation. In the excess analysis for each near-infrared colour, ten of the fifteen known variable L3–L7 dwarfs have above-average silicate strengths, as seen from the right three panels of Figure 11. Among the 12 non-variables, seven are below average in all colour excess combinations. The former occurrence is significant at the 85 per cent level, whereas the latter is consistent with being random.

Overall, we find a probable (98.8 per cent) indication that variable L3–L7 dwarfs are ≈ 2 times more likely to exhibit above-average silicate absorption than non-variable L3–L7 dwarfs (11/15 for variables vs. 4/12 for non-variables). If dependence on spectral type in the L3–L7 range is ignored and only near-infrared colour excess is considered, the significance of the correlation is weaker (85 per cent). The probable link between variability and silicate absorption strength affirms earlier suggestions (Burgasser et al. 2002; Marley et al. 2010) that the clouds responsible for photometric variability in L dwarfs are composed of silicates.

4 SUMMARY AND CONCLUSIONS

We have reprocessed and presented $R \approx 90$ mid-infrared spectra of all 113 field M5–T9 dwarfs observed and detected with the *Spitzer* IRS. These include 12 M5–M9 dwarfs, 69 L dwarfs, and 32 T dwarfs (Table 1). Spectra for 68 of the 113 (i.e., 60 per cent) detected field M5–T9 dwarfs are presented here for the first time, although 32 of the 68 spectra are mentioned in previous references without being shown or available (Table 2). Most of the spectra cover the 5.2–14.2 μm wavelength range, except for the spectra of the five latest T dwarfs, which cover 7.5–14.2 μm (Figures 1, 2, and 3). Eighteen of the spectra have coverage that extends up to 38 μm (Figure 4).

We have analysed the strengths of the main mid-infrared molecular and condensate absorbers, namely H_2O at 6.25 μm , CH_4 at 7.65 μm , NH_3 at 10.5 μm , and silicates at 8–11 μm . Water absorption is present in all spectra and strengthens with increasing spectral type. Methane and ammonia features appear consistently at L8 and T2.5, respectively, although ammonia may be discernible as early as T1.5. These findings are consistent with the analysis of select M, L, and T IRS spectra from Cushing et al. (2006), and improve the robustness of these early results.

Our uniform analysis of all field M5–T9 IRS spectra traces for the

first time the emergence and sedimentation of silicate condensates in L dwarfs. To this end we design an index to measure the strength of the 8–11 μm flux deficit previously attributed to silicate absorption in select L dwarfs. Our analysis, bound by the S/N ratio and resolution limits of the archival *Spitzer* IRS spectra, shows that silicate condensates first attain measurable optical depth in the visible atmosphere of ultracool dwarfs at spectral type L2 ($T_{\text{eff}} = 1960$ K), are thickest between L4–L6 ($1690 \text{ K} \geq T_{\text{eff}} \geq 1480$ K), and sediment below the 8–11 μm photosphere past spectral type L8 ($T_{\text{eff}} = 1340$ K; bottom panel of Figure 6). However, at any L subtype silicate absorption can also be absent from the IRS spectra, even for mid-L dwarfs.

Objects with the strongest silicate absorption are preferentially redder in the near-infrared compared to other dwarfs with similar spectral types (Figure 9). Specifically, there is a significant correlation between the silicate absorption strength and the deviation from median near-infrared 2MASS colours (colour excess) of L3–L7 dwarfs (Figure 10), as suggested in previous studies (Burgasser et al. 2008a; Cushing et al. 2008;Looper et al. 2008). A similar positive correlation holds, but with less significance, for all L dwarfs with IRS spectra. This result is consistent with the scenario in which variations of condensate cloud thickness produce the observed colour scatter at a fixed subtype in L dwarfs (Knapp et al. 2004; Burgasser et al. 2008a; Cushing et al. 2008; Looper et al. 2008).

Variable mid-L dwarfs exhibit on average stronger silicate absorption than non-variables with similar spectral types or 2MASS colour excesses (Figure 11). Conversely, L3–L7 dwarfs with above-average silicate absorption are approximately twice more likely to be photometrically variable.

The consistent detection of silicate absorption in the IRS L dwarf sample, its progression in strength, its correlation with near-infrared colour excess, and its ≈ 99 per cent probable link to photometric variability, solidify the evidence that: (1) silicates condense to form clouds in L dwarf atmospheres, (2) these silicate clouds govern L-dwarf variability, and (3) they are responsible for the observed colour scatter in L dwarfs. The photometric variability of early T dwarfs is also likely caused by silicate clouds, but the lack of detectable silicate absorption in early-T IRS spectra indicates that the silicates have sedimented to higher pressure levels than the $\lesssim 1$ bar probed in the 8–11 μm wavelength range.

There are many other possible applications of the *Spitzer* IRS spectroscopic sample presented here (e.g.; Cushing et al. 2006; Birmingham et al. 2021; Suárez et al. 2021). We expect that this sample will be used in future studies to improve our understanding of the atmospheric physics and chemistry of ultracool dwarfs, and will serve as a basis for planning and interpreting ultracool dwarf and exoplanet observations with the *James Webb Space Telescope*.

ACKNOWLEDGEMENTS

We thank Theodora Karalidi for providing an extended (to 25 μm) version of the plot of probed atmospheric pressure vs. wavelength published in Karalidi et al. (2021). Support for this work was provided by the Canadian Space Agency under the 2019 announcement of opportunity for the Flights and Fieldwork for the Advancement of Science and Technology (FAST-AO 2019) programme (reference no. 19FAWESB40). The spectra presented here are obtained entirely with the *Spitzer* Space Telescope, which is operated by the Jet Propulsion Laboratory, California Institute of Technology under a contract with NASA. This work has benefitted from The UltracoolSheet, maintained by Will Best, Trent Dupuy, Michael Liu, Rob Siverd, and

Zhoujian Zhang, and developed from compilations by Dupuy & Liu (2012), (Dupuy & Kraus 2013), Liu et al. (2016), Best et al. (2018), and Best et al. (2021).

DATA AVAILABILITY

The data underlying this article are available in the article and in its online supplementary material and on Genaro Suárez' homepage⁷.

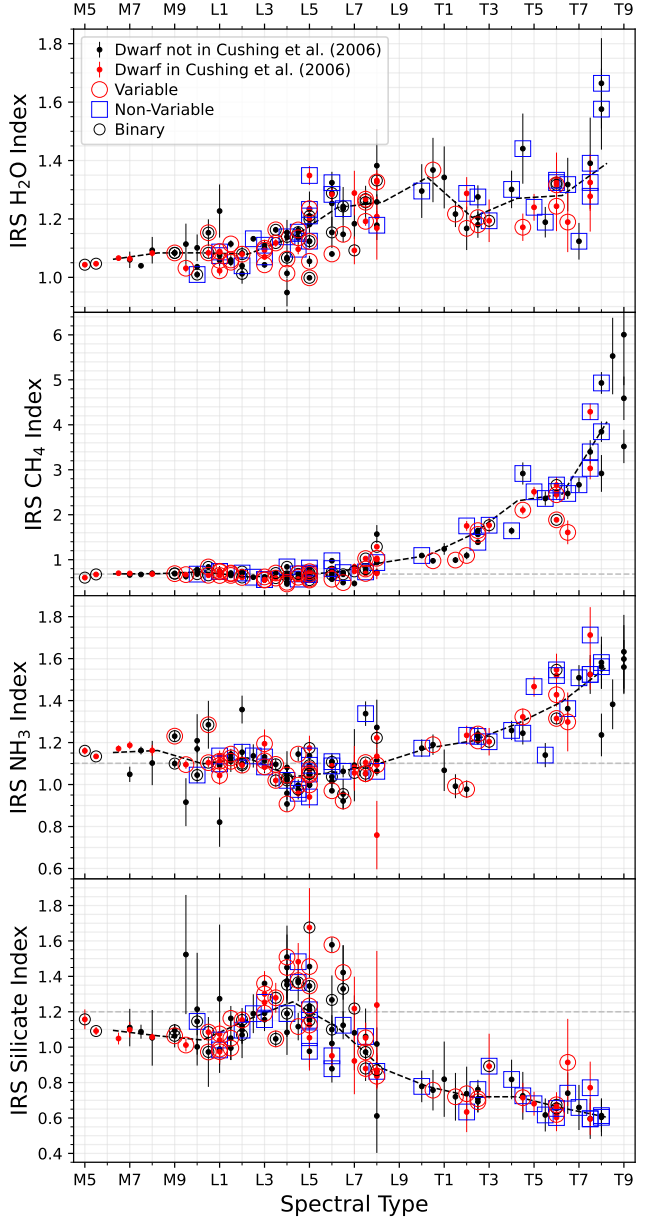


Figure 6. The H_2O , CH_4 , NH_3 , and silicate indices from the IRS spectra as a function of spectral type. The dwarfs included in the Cushing et al. (2006) list are shown with red points; the dwarfs absent from that reference are shown with black points. The red circles, blue squares, and black circles indicate variable, non-variable, and binary sources (Table 1), respectively. The dashed black curve in each panel traces the median spectral index in bins of two spectral subtypes. The dashed grey line in the middle panels is a reference for the onset of the methane and ammonia absorption bands and is obtained as the median index value for $\leq \text{L}5$ -type (where the features are clearly absent in the IRS spectra) objects. The dashed grey line in the bottom panel shows the threshold above which we selected sources with the largest silicate index values.

⁷ <https://gsuarezcastro.wixsite.com/gsuarez/research>

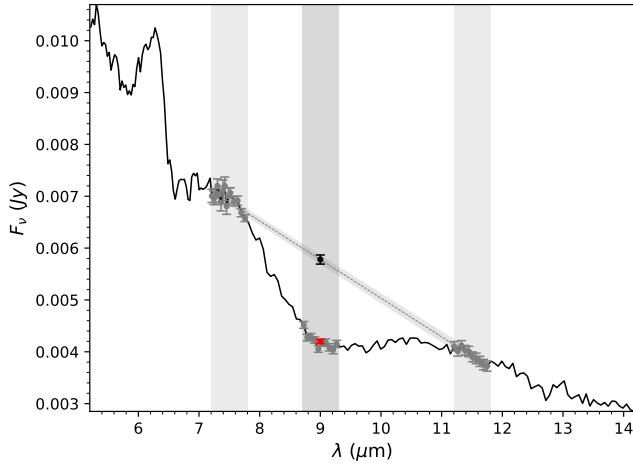


Figure 7. Example of how the silicate index was measured considering the IRS spectrum of the L4.5 dwarf 1821+1414. The shaded regions show the windows used to measure the silicate index (dark grey for the absorption and light grey for fitting the continuum). The black point indicates the interpolated continuum flux at $9.0 \mu\text{m}$ obtained by considering the best linear fit (black dashed line with uncertainties shown by the diagonally shaded region) to the fluxes at 7.5 and $11.5 \mu\text{m}$ in a window of $0.6 \mu\text{m}$ (grey points). The red point corresponds to the average flux at $9.0 \mu\text{m}$ in a same-width window (grey points). The silicate index is defined as the ratio of the interpolated continuum flux to the absorption flux.

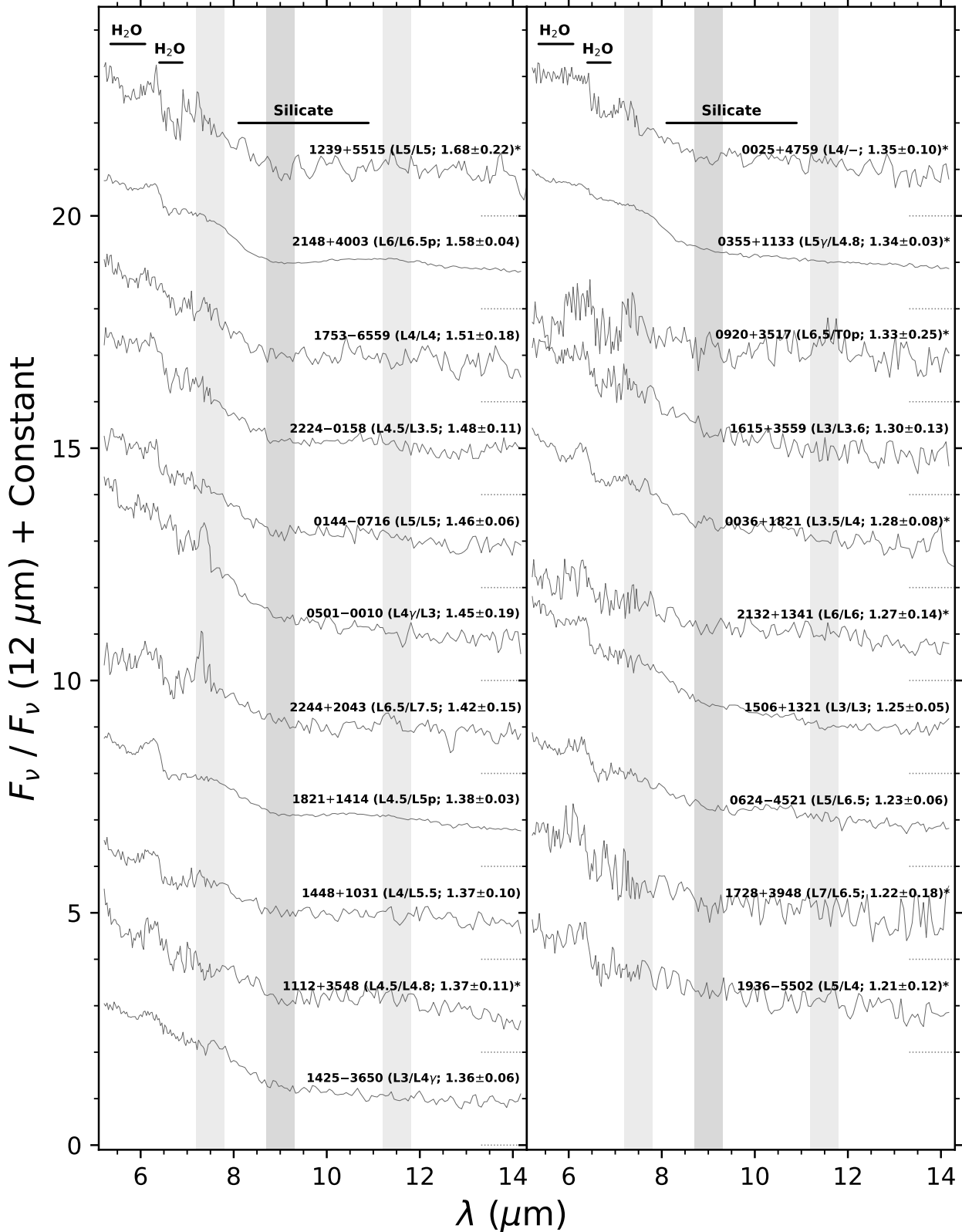


Figure 8. IRS spectra of the dwarfs with the largest silicate index values (≥ 1.2 and fractional errors < 20 per cent). The selected dwarfs have (adopted optical) spectral types between L3 and L7. Optical and near-infrared spectral types (when available) are indicated for each object, as is the silicate index value and its uncertainty. The spectra were normalised to unity using the median flux at $12 \mu\text{m}$ in a $0.6 \mu\text{m}$ window and offset by constants (dotted lines). The shaded regions show the windows used to measure the silicate index (dark grey for the absorption and light grey for fitting the continuum). The spectra are ordered by decreasing silicate index from the top left to the bottom right. Unresolved binaries are marked with asterisks (Table 1).

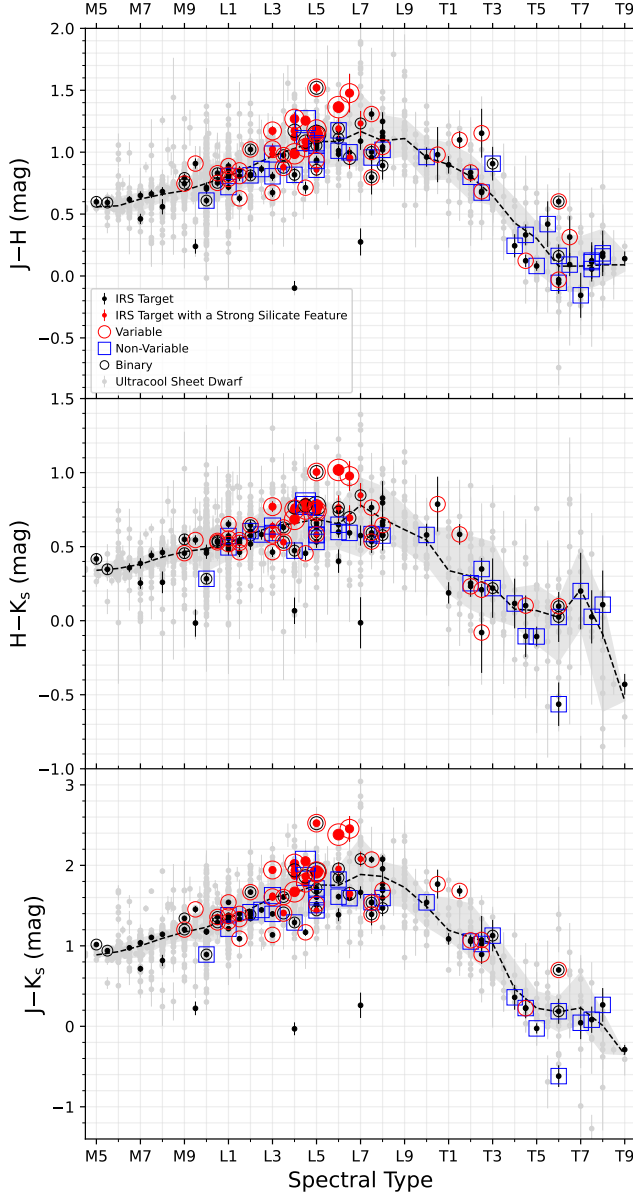


Figure 9. Near-infrared 2MASS colours as a function of spectral type for all >2000 M5–T9 dwarfs in the UltracoolSheet catalogue (grey points). All field M5–T9 dwarfs with IRS spectra and 2MASS photometry are shown in with black points, while those with the largest silicate index values (see Fig. 6, bottom panel) are shown with red points (with the symbol size proportional to the index value). The red circles, blue squares, and black circles indicate variable, non-variable, and binary sources (Table 1), respectively. The dashed curve and the shaded area in each panel represent the median index and 68 per cent central confidence interval for all dwarfs in the UltracoolSheet catalogue, calculated in bins of one spectral subtype.

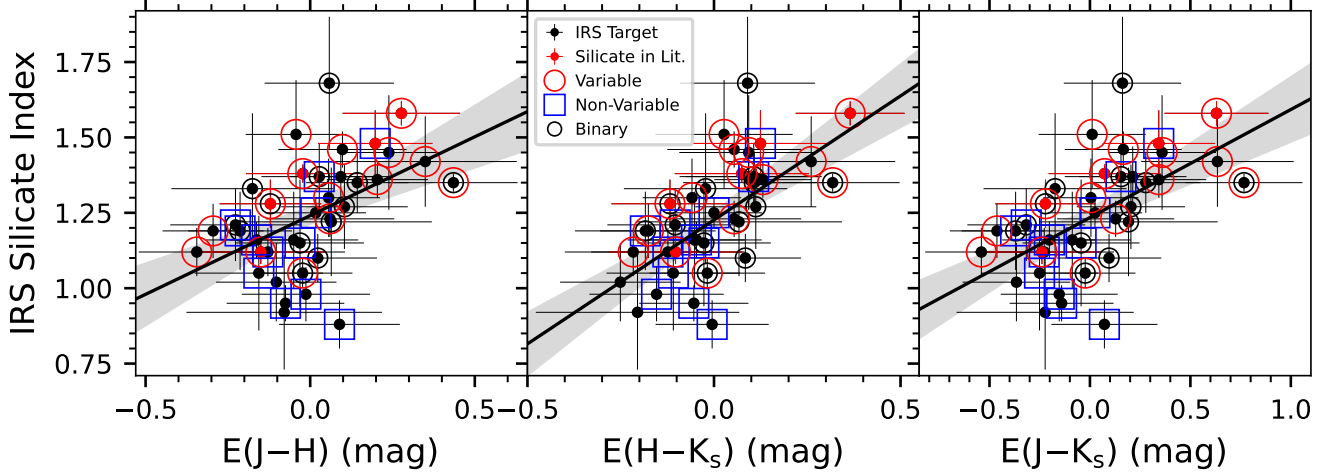


Figure 10. Silicate index as a function of 2MASS colour excess (Section 3.2.2) for 37 of the 39 L3–L7 dwarfs with IRS spectra. Among these, the red points indicate the five mid-L objects with previously-reported silicate absorption: 0036+1821 (L3.5), 1507–1627 (L5), and 2224–0158 (L4.5) in Cushing et al. (2006), and 1821+1414 (L4.5) and 2148+4003 (L6) inLooper et al. (2008). The red circles, blue squares, and black circles indicate variable, non-variable, and binary sources (Table 1), respectively. The best linear fit to the data points in each panel is indicated by the black line. The shaded region represents the 1σ uncertainties of the fit in both slope and intercept. We excluded the subdwarfs 0532+8246 (sdL7) and 1626+3925 (sdL4) that have very blue 2MASS colours (e.g., $J - K_s < 0.5$ mag; Figure 9).

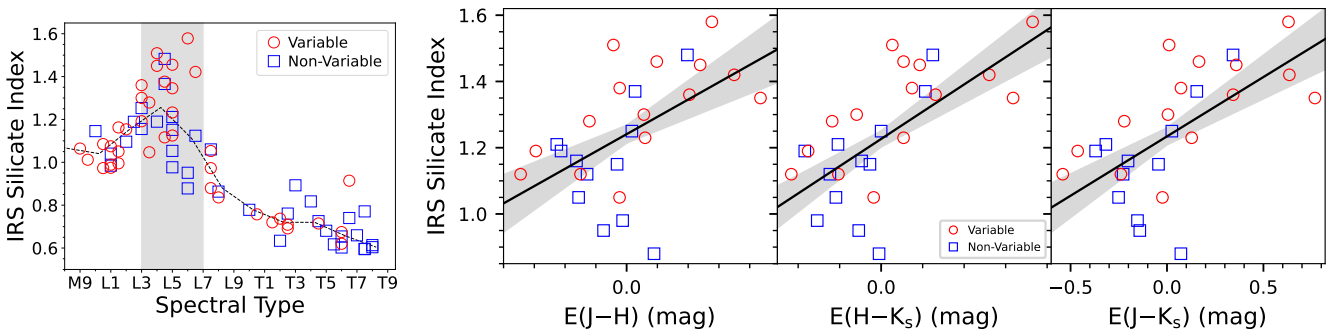


Figure 11. Silicate index as a function of spectral type (left panel) or near-infrared 2MASS colour excess (right three panels) for variable (red circles) and non-variable (blue squares) ultracool dwarfs with IRS spectra (Table 1). The shaded region in the left panel indicate the L3–L7 spectral type range where we focus the analysis on variability. The dashed curve in the left panel, and the solid line and shaded region in the right three panels, are the same as in Figures 6 (bottom panel) and 10, respectively. The right three panels focus on L3–L7 dwarfs, for which the presented assessment of variability and non-variability from the published literature is complete. We have excluded the two L subdwarfs (1626+3925 and 0532+8246), as explained in Section 3.2.2.

Table 1: Select properties of the 113 field M5–T9 dwarfs with detectable signal in *Spitzer* IRS spectra.

Designation	Short Name (hhmm±ddmm)	Other Name	R.A._J2000 (°)	Decl._J2000 (°)	Discovery Ref.	SpT _{opt}	Ref.	SpT _{IR}	Ref.	Binary	Variable	Non-Variable
2MASS J00001354+2554180	0000+2554	...	0.0563	25.9055	Knap04	T5	Pine16	T4.5	Burg06b	Buen14
2MASS J00043484–4044058	0004–4044	GJ 1001BC, LHS 102BC	1.1453	–40.7351	EROS99	L5	Kirk01	L4.5	Knap04	Goli04	...	Diet14
2MASS J00242463–0158201	0024–0158	DY Psc, BRI 0021-0214	6.1026	–1.9722	Irwi91	M9.5	Kirk95	M9.5	Geba02	...	Mart01	...
2MASS J00250365+4759191	0025+4759	...	6.2654	47.9886	Cruz07	L4	Cruz07	Reid06
ULAS J003402.77–005206.7	0034–0052	...	8.5116	–0.8690	Warr07	T9	Burn08
2MASS J00345157+0523050	0034+0523	...	8.7144	5.3846	Burg04b	T6.5	Burg06b	Wils14
2MASS J00361617+1821104	0036+1821	...	9.0671	18.3529	Reid00	L3.5	Kirk00	L4	Knap04	Bern10	Metc15	...
CFBDS J005910–011401	0059–0114	...	14.7963	–1.2336	Delo08	T9	Delo08
2MASS J01365662+0933473	0136+0933	SIMP J013656.5+093347.3	24.2357	9.5631	Arti06	T2	Pine16	T2.5	Arti06	...	Arti09	...
2MASS J01390120–1757026	0139–1757	Gl 65, G 272-61	24.7557	–17.9507	Luyt49	M5.5	Kirk91	Kirk91
2MASS J01443536–0716142	0144–0716	...	26.1475	–7.2706	Lieb03	L5	Lieb03	L5	Maro13	...	Koen13	...
2MASS J02511490–0352459	0251–0352	...	42.8157	–3.8854	Cruz03	L3	Cruz03	L1	Wils03	Koen13
2MASS J02550357–4700509	0255–4700	...	43.7654	–47.0143	Mart99	L8	Kirk08	L9	Burg06b	...	Mora06	...
2MASS J03552337+1133437	0355+1133	...	58.8474	11.5622	Reid06	L5γ	Cruz09	L4.8	Bard14	Bern10	Vos22	...
2MASS J04151954–0935066	0415–0935	...	63.8386	–9.5835	Burg02	T8	Burg03d	T8	Burg06b	Radi14
2MASS J04234858–0414035	0423–0414	...	65.9524	–4.2342	Geba02	L7.5	Cruz03	T0	Burg06b	Burg05b	Kao18	...
2MASS J04291842–3123568	0429–3123	...	67.3269	–31.3991	Cruz03	M7.5	Cruz03
2MASS J04390101–2353083	0439–2353	...	69.7542	–23.8857	Cruz03	L6.5	Cruz03	L6	Burg10	Koen13
2MASS J04455387–3048204	0445–3048	...	71.4746	–30.8057	Cruz03	L2	Cruz03	Koen13
2MASS J05012406–0010452	0501–0010	...	75.3504	–0.1793	Reid08	L4γ	Cruz09	L3	Alle13	...	Vos20	...
2MASS J05233822–1403022	0523–1403	...	80.9093	–14.0506	Cruz03	L2.5	Cruz03	L5	Wils03	Koen13
2MASS J05325346+8246465	0532+8246	...	83.2268	82.7792	Burg03c	sdL7	Burg07	sdL	Burg03c
2MASS J05395200–0059019	0539–0059	...	84.9667	–0.9837	Fan00	L5	Fan00	L5	Knap04	Koen13
2MASS J05591914–1404488	0559–1404	...	89.8300	–14.0803	Burg00a	T5	Burg03d	T4.5	Burg06b	...	Radi14	...
2MASS J06244595–4521548	0624–4521	...	96.1914	–45.3652	Reid08	L5	Reid08	L6.5	Schn14	...	Buen14	...
2MASS J07003664+3157266	0700+3157	...	105.1530	31.9571	Thor03	L3.5	Thor03	Reid06	Mile17	...
2MASS J07271824+1710012	0727+1710	...	111.8298	17.1643	Burg02	T8	Burg03d	T7	Burg06c	Gira13
2MASS J07464256+2000321	0746+2000	...	116.6754	20.0087	Reid00	L0.5	Kirk00	L1	Knap04	Reid01	Hard13	...
2MASS J07584037+3247245	0758+3247	...	119.6670	32.7886	Knap04	T3	Pine16	T2	Burg06b	...	Radi14	...
2MASS J08053189+4812330	0805+4812	...	121.3827	48.2091	Hawl02	L4	Hawl02	L9	Knap04	Dupu12	...	Gira13
2MASS J08251968+2115521	0825+2115	...	126.3317	21.2643	Kirk00	L7.5	Kirk00	L6	Knap04	...	Metc15	...
2MASS J08294949+2646348	0829+2646	GJ 1111, LHS 248	127.4556	26.7760	Boes76	M6.5	Kirk91
2MASS J08300825+4828482	0830+4828	...	127.5274	48.4765	Geba02	L8	Kirk08	L9	Geba02
SDSS J083717.21–000018.0	0837–0000	...	129.3215	–0.0051	Legg00	T0	Kirk08	T1	Burg06b
2MASS J08575849+5708514	0857+5708	...	134.4937	57.1476	Geba02	L8	Kirk08	L8	Geba02
2MASS J09083803+5032088	0908+5032	...	137.1584	50.5356	Cruz03	L5	Cruz03	L9	Knap04	Buen14
2MASS J09111297+7401081	0911+7401	...	137.8040	74.0189	Reid08	L0	Reid08
2MASS J09121469+1459396	0912+1459	Gl 337CD, pi.01 Cnc C	138.0608	14.9946	Wils01	L8	Wils01	T0	Burg06b	Burg05a
2MASS J09201223+3517429	0920+3517	...	140.0509	35.2952	Kirk00	L6.5	Kirk00	T0p	Burg06b	Dupu12
2MASS J09211410–2104446	0921–2104	...	140.3088	–21.0790	Reid08	L1.5	Reid08	L4	Burg08a	...	Koen13	...
2MASS J09293364+3429527	0929+3429	...	142.3901	34.4980	Kirk00	L8	Kirk00	L7.5	Knap04
2MASS J09373487+2931409	0937+2931	...	144.3985	29.5242	Burg02	T7	Burg03d	T6p	Burg06b	Gira13
2MASS J09393548–2448279	0939–2448	...	144.8997	–24.8108	Tinn05	T8	Pine16	T8	Burg06b	Radi14
2MASS J10130734–1356204	1013–1356	...	153.2806	–13.9393	Scho04	sdM9.5	Scho04
2MASS J10170754+1308398	1017+1308	...	154.2815	13.1444	Cruz03	L2	Cruz03	L1	Wils03	Gizi03

Table 1 – (Continued)

Designation	Short Name (hhmm±ddmm)	Other Name	R.A. _{J2000} (°)	Decl. _{J2000} (°)	Discovery Ref.	SpT _{opt}	Ref.	SpT _{IR}	Ref.	Binary	Variable	Non-Variable
2MASS J10210969–0304197	1021–0304	...	155.2904	−3.0723	Legg00	T3.5	Kirk08	T3	Burg06b	Burg06a	...	Wils14
2MASS J10224821+5825453	1022+5825	...	155.7009	58.4293	Reid08	L1β	Cruz09	L0.6	Bard14
CFBDS J102841+565401	1028+5654	...	157.1709	56.9005	Albe11	T8.0	Albe11
2MASS J10365305–3441380	1036–3441	...	159.2211	−34.6940	Gizi02	L6	Gizi02	L6.5	Burg10	Radi14
2MASS J10452400–0149576	1045–0149	...	161.3499	−1.8327	Gizi02	L1	Gizi02	L2	Maro13	Koen13
2MASS J10484281+0111580	1048+0111	...	162.1784	1.1995	Hawl02	L1	Hawl02	L4	Kend04	...	Koen03	...
2MASS J10511900+5613086	1051+5613	...	162.8291	56.2191	Reid08	L2	Reid08	L0.8	Bard14
2MASS J10521350+4422559	1052+4422	...	163.0561	44.3822	Chiu06	L7.5	Pine16	T0.5	Chiu06	Dupu15	Gira13	...
2MASS J11061197+2754225	1106+2754	...	166.5484	27.9041	Loop07	T2.5	Loop07	Gira13
2MASS J11083081+6830169	1108+6830	...	167.1282	68.5046	Gizi00	L1e	Gizi00	L1.8	Alle16	...	Clar02b	...
2MASS J11101001+0116130	1110+0116	...	167.5417	1.2702	Geba02	T5.5	Burg06b	Radi14
2MASS J11122567+3548131	1112+3548	HD 97334B, Gl 417BC	168.1068	35.8035	Kirk00	L4.5	Kirk00	L4.8	Bard14	Bouy03	...	Bail03
2MASS J11145133–2618235	1114–2618	...	168.7031	−26.3078	Tinn05	T8	Pine16	T7.5	Burg06b	Radi14
2MASS J11263991–5003550	1126–5003	...	171.6658	−50.0652	Folk07	L4.5	Burg08a	L6.5p	Burg08a	...	Metc15	...
2MASS J11555389+0559577	1155+0559	...	178.9727	5.9991	Knap04	L7.5	Knap04	Radi14
2MASS J12074717+0244249	1207+0244	...	181.9444	2.7408	Hawl02	L8	Hawl02	T0	Burg06b	Radi14
2MASS J12130336–0432437	1213–0432	...	183.2639	−4.5455	Cruz03	L5	Cruz03	L4.2	Bard14
2MASS J12171110–0311131	1217–0311	...	184.2958	−3.1869	Burg99	T7	Burg03d	T7.5	Burg06b	Radi14
2MASS J12255432–2739466	1225–2739	...	186.4767	−27.6637	Burg99	T6	Burg03d	T6	Burg06b	Burg03b	...	Wils14
2MASS J12373919+6526148	1237+6526	...	189.4056	65.4356	Burg99	T7	Burg03d	T6.5	Burg06b	...	Kao18	...
2MASS J12392727+5515371	1239+5515	...	189.8637	55.2603	Kirk00	L5	Kirk00	L5	Schn14	Gizi03
2MASS J12545393–0122474	1254–0122	...	193.7246	−1.3798	Legg00	T2	Burg03d	T2	Burg06b	Gira13
2MASS J13054019–2541059	1305–2541	Kelu-1, Kelu-1AB	196.4174	−25.6850	Ruiz97	L2	Kirk99	L0.5p	Stum08	Liu05	Clar02	...
2MASS J13314894–0116500	1331–0116	...	202.9539	−1.2809	Hawl02	L6	Hawl02	L6	Maro15
ULAS J133553.45+113005.2	1335+1130	...	203.9725	11.5013	Burn08	T9	Burn08
2MASS J14252798–3650229	1425–3650	...	216.3666	−36.8398	Kend04	L3	Reid08	L4γ	Gagn15	...	Radi14	...
2MASS J14390030+1839385	1439+1839	LHS 377	219.7512	18.6608	Legg96	sdM7	Gizi97
2MASS J14392836+1929149	1439+1929	...	219.8634	19.4889	Kirk99	L1	Kirk99	L1	Schn14	Bail01
2MASS J14413716–0945590	1441–0945	...	220.4049	−9.7664	Mart99	L0.5	Kirk08	L0.4	Bard14	Bouy03	Bail04	...
2MASS J14482563+1031590	1448+1031	...	222.1068	10.5331	Wils03	L4	Reid08	L5.5	Schn14
2MASS J14563831–2809473	1456–2809	LHS 3003, LP 914-54	224.1594	−28.1635	Bess91	M7	Kirk95	M7	Geba02
2MASS J14571496–2121477	1457–2121	Gl 570D	224.3160	−21.3689	Burg00b	T7	Burg03d	T7.5	Burg06b	Koen04
2MASS J15031961+2525196	1503+2525	...	225.8317	25.4222	Burg03a	T6	Burg03d	T5	Burg06b	Gira13
2MASS J15065441+1321060	1506+1321	...	226.7264	13.3517	Gizi00	L3	Gizi00	L3	Schn14	Geli02
2MASS J15074769–1627386	1507–1627	...	226.9486	−16.4611	Reid00	L5	Kirk00	L5.5	Knap04	...	Metc15	...
2MASS J15150083+4847416	1515+4847	...	228.7474	48.8011	Wils03	L6	Cruz07	L6.5	Cruz03	Buen14
2MASS J15164306+3053443	1516+3053	...	229.1791	30.8957	Chiu06	T0.5	Chiu06	...	Metc15	...
2MASS J15203974+3546210	1520+3546	...	230.1673	35.7709	Chiu06	T0	Chiu06	Metc15
2MASS J15232263+3014562	1523+3014	Gl 584C, eta CrB C	230.8443	30.2489	Kirk00	L8	Kirk00	L8	Geba02
2MASS J15261405+2043414	1526+2043	...	231.5584	20.7279	Kirk00	L7	Kirk00	L5	Schn14
2MASS J16102900–0040530	1610–0040	...	242.6206	−0.6816	Lepi03	sdL	Lepi03	sdM7	Burg07	Dahn08	...	Koen13
2MASS J16154416+3559005	1615+3559	...	243.9340	35.9832	Kirk00	L3	Kirk00	L3.6	Bard14	...	Bail04	...
2MASS J16241436+0029158	1624+0029	...	246.0597	0.4877	Stra99	T6	Pine16	T6	Burg06b	...	Buen14	...
2MASS J16262034+3925190	1626+3925	...	246.5839	39.4221	Burg04a	sdL4	Burg07	sdL	Burg04a
2MASS J16580380+7027015	1658+7027	...	254.5158	70.4505	Gizi00	L1	Gizi00	Geli02
2MASS J17072343–0558249	1707–0558	...	256.8476	−5.9737	Gizi02	M9	Gizi02	M9	McEl06	Reid06
2MASS J17210390+3344160	1721+3344	...	260.2651	33.7380	Cruz03	L3	Cruz03	L5	Burg08a	...	Metc15	...

Table 1 – (Continued)

Designation	Short Name (hhmm±ddmm)	Other Name	R.A. _{J2000} (°)	Decl. _{J2000} (°)	Discovery Ref.	SpT _{opt}	Ref.	SpT _{IR}	Ref.	Binary	Variable	Non-Variable
2MASS J17281150+3948593	1728+3948	...	262.0479	39.8165	Kirk00	L7	Kirk00	L6.5	Schn14	Gizi03
2MASS J17312974+2721233	1731+2721	...	262.8739	27.3565	Reid08	L0	Reid08	L0	Alle13
2MASS J17534518–6559559	1753–6559	...	268.4383	-65.9988	Reid08	L4	Reid08	L4	Maro13	...	Metc15	...
2MASS J18071593+5015316	1807+5015	...	271.8164	50.2588	Cruz03	L1.5	Cruz03	L1	Wils03	...	Mile17	...
2MASS J18212815+1414010	1821+1414	...	275.3673	14.2336	Loop08	L4.5	Loop08	L5p	Kirk10	...	Metc15	...
2MASS J18284076+1229207	1828+1229	...	277.1698	12.4891	Kirk10	M8p	Kirk10	M7.5p	Kirk10
2MASS J19165762+0509021	1916+0509	Gl 752B, VB 10	289.2401	5.1506	vanB61	M8	Henr90	M8	Bard14
2MASS J19360187–5502322	1936–5502	...	294.0079	-55.0423	Reid08	L5	Reid08	L4	Maro13	Pope13	...	Koen13
2MASS J20575409–0252302	2057–0252	...	314.4754	-2.8751	Cruz03	L1.5	Cruz03	L1.5	Kend04	...	Koen13	...
2MASS J21321145+1341584	2132+1341	...	323.0477	13.6995	Cruz07	L6	Cruz07	L6	Schn14	Sieg07
2MASS J21392676+0220226	2139+0220	...	324.8629	2.3400	Reid08	T2	Pine16	T1.5	Burg06b	...	Radi12	...
2MASS J21442847+1446077	2144+1446	HN Peg B	326.1188	14.7688	Luhm07a	T2.5	Luhm07a	...	Zhou18	...
ULAS J214638.83–001038.7	2146–0010	Wolf 940 B	326.6628	-0.1776	Burn09	T8.5	Burn09
2MASS J21481633+4003594	2148+4003	...	327.0679	40.0665	Loop08	L6	Loop08	L6.5p	Kirk10	...	Metc15	...
2MASS J21522609+0937575	2152+0937	...	328.1087	9.6326	Reid06	L6	Reid08	Reid06
2MASS J22041052–5646577	2204–5646	eps Ind B, eps Indi Ba/Bb	331.0656	-56.7901	Scho03	T6	Burg06b	McCa04	Koen03	...
2MASS J22244381–0158521	2224–0158	...	336.1827	-1.9815	Kirk00	L4.5	Kirk00	L3.5	Knap04	Koen13
2MASS J22383372–1517573	2238–1517	Gl 866, L789-6	339.6408	-15.3008	Lein86	M5	Kirk91	Lein86
2MASS J22443167+2043433	2244+2043	...	341.1322	20.7285	Dahn02	L6.5	Kirk08	L7.5	Knap04	...	Vos18	...
2MASS J22541892+3123498	2254+3123	...	343.5788	31.3972	Burg02	T5	Pine16	T4	Burg06b	Radi14
2MASS J23515044–2537367	2351–2537	...	357.9603	-25.6269	Poko04	M9	Lodi05	M8	Burg08b	Bart17	Koen13	...

References. Albe11: Albert et al. (2011), Alle13: Allers & Liu (2013), Alle16: Aller et al. (2016), Arti06: Artigau et al. (2006), Arti09: Artigau et al. (2009), Bail01: Bailer-Jones & Mundt (2001), Bail03: Bailer-Jones & Lamm (2003), Bail04: Bailer-Jones (2004), Bard14: Bardalez Gagliuffi et al. (2014), Bart17: Bartlett et al. (2017), Bern10: Bernat et al. (2010), Bess91: Bessell (1991), Boes76: Boeshaar (1976), Bouy03: Bouy et al. (2003), Buen14: Buenzli et al. (2014), Burg99: Burgasser et al. (1999), Burg00a: Burgasser et al. (2000a), Burg00b: Burgasser et al. (2000b), Burg02: Burgasser et al. (2002), Burg03a: Burgasser et al. (2003a), Burg03b: Burgasser et al. (2003b), Burg03c: Burgasser et al. (2003c), Burg03d: Burgasser et al. (2003d), Burg04a: Burgasser (2004), Burg04b: Burgasser et al. (2004), Burg05a: Burgasser et al. (2005a), Burg05b: Burgasser et al. (2005b), Burg06a: Burgasser et al. (2006a), Burg06b: Burgasser et al. (2006b), Burg06c: Burgasser et al. (2006c), Burg07: Burgasser et al. (2007), Burg08a: Burgasser et al. (2008a), Burg08b: Burgasser et al. (2008b), Burg08b: Burgasser et al. (2008b), Burg10: Burgasser et al. (2010), Burn08: Burningham et al. (2008), Burn09: Burningham et al. (2009), Chiu06: Chiu et al. (2006), Clar02: Clarke et al. (2002a), Clar02b: Clarke et al. (2002b), Cruz03: Cruz et al. (2003), Cruz07: Cruz et al. (2007), Cruz09: Cruz et al. (2009), Dahn02: Dahn et al. (2002), Dahn08: Dahn et al. (2008), Delo08: Delorme et al. (2008), Diet14: Dieterich et al. (2014), Dupu12: Dupuy & Liu (2012), Dupu15: Dupuy et al. (2015), EROS99: EROS Collaboration et al. (1999), Fan00: Fan et al. (2000), Folk07: Folkes et al. (2007), Gagn15: Gagné et al. (2015), Geba02: Geballe et al. (2002), Geli02: Gelino et al. (2002), Gira13: Girardin et al. (2013), Gizi97: Gizis (1997), Gizi00: Gizis et al. (2000), Gizi02: Gizis (2002), Gizi03: Gizis et al. (2003), Goli04: Goliowski et al. (2004), Hard13: Harding et al. (2013), Hawl02: Hawley et al. (2002), Henr90: Henry & Kirkpatrick (1990), Irwi91: Irwin et al. (1991), Kao18: Kao et al. (2018), Kendall04: Kendall et al. (2004), Kirk91: Kirkpatrick et al. (1991), Kirk95: Kirkpatrick et al. (1995), Kirk99: Kirkpatrick et al. (1999), Kirk00: Kirkpatrick et al. (2000), Kirk01: Kirkpatrick et al. (2001), Kirk08: Kirkpatrick et al. (2008), Kirk10: Kirkpatrick et al. (2010), Knap04: Knapp et al. (2004), Koen03: Koen (2003), Koen04: Koen et al. (2004), Koen13: Koen (2013), Legg96: Leggett et al. (1996), Legg00: Leggett et al. (2000), Lein86: Leinert et al. (1986), Lepi03: Lépine et al. (2003b), Lieb03: Liebert et al. (2003), Liu05: Liu & Leggett (2005), Lodi05: Lodieu et al. (2005), Loop07:Looper et al. (2007), Loop08:Looper et al. (2008), Luhm07a: Luhman et al. (2007a), Luyt49: Luyten (1949), Mile17: Miles-Páez et al. (2017a), Maro13: Marocco et al. (2013), Maro15: Marocco et al. (2015), Mart99: Martín et al. (1999), Mart01: Martín et al. (2001), McCa04: McCaughean et al. (2004), McEl06: McElwain & Burgasser (2006), Metc15: Metchev et al. (2015), Mora06: Morales-Calderón et al. (2006), Pine16: Pineda et al. (2016), Poko04: Pokorny et al. (2004), Pope13: Pope et al. (2013), Radi12: Radigan et al. (2012), Radi14: Radigan et al. (2014), Reid00: Reid et al. (2000), Reid01: Reid et al. (2001), Reid06: Reid et al. (2006), Reid08: Reid et al. (2008), Ruiz97: Ruiz et al. (1997), Schn14: Schneider et al. (2014), Scho03: Scholz et al. (2003), Scho04: Scholz et al. (2004), Sieg07: Siegler et al. (2007), Stra99: Strauss et al. (1999), Stum08: Stumpf et al. (2008), Thor03: Thorstensen & Kirkpatrick (2003), Tinn05: Tinney et al. (2005), vanB61: Van Biesbroeck (1961), Vos18: Vos et al. (2018), Vos20: Vos et al. (2020), Vos22: Vos et al. (2022), Warr07: Warren et al. (2007), Wils01: Wilson et al. (2001), Wils03: Wilson et al. (2003), Wils14: Wilson et al. (2014), Zhou18: Zhou et al. (2018). (This table is available in machine-readable form in the online supplementary data.)

Table 2: Log of the *Spitzer* IRS observations of the 113 field M5–T9 dwarfs with detectable signal.

Dwarf	Prog. ID	AOR KEY (hhmm±ddmm)	Modules	Exposure Time				Obs. Date (UT; YYYY/MM/DD)	PI	S/N at		Publication Reference ¹
				SL2	SL1	LL2	LL1	(min)		6 μm	12 μm	
0000+2554	20514	14796032, 14796288	SL2,SL1	144	200	2005-12-18, 2006-01-25	Golimowski, David A.	15	11	Step09
0004-4044	50367	26090752	SL2,SL1	2	3	2009-01-15	Cushing, Michael C.	14	4	Suar22
0024-0158	29	3877632	SL2,SL1,LL2	2	4	36	...	2004-01-04	Houck, James R.	26	9	Cush06
0025+4759	50367	26090496	SL2,SL1	16	30	2009-03-07	Cushing, Michael C.	20	7	Fili15, Suar22
0034-0052	40419	21830400, 21830656	SL1	...	512	2008-01-15	Leggett, Sandy K.	...	9	Legg09
0034+0523	20544	14825728	SL2,SL1	120	120	2006-01-19	Burgasser, Adam J.	9	12	Suar22
0036+1821	51	4188672	SL2,SL1,LL2,LL1	8	8	8	16	2004-01-06	Houck, James R.	37	11	Cush06
0059-0114	50667	26685440	SL1	...	238	2009-01-13	Albert, Loic	...	13	Suar22
0136+0933	40076	21967104	SL2,SL1	6	6	2008-09-01	Mainzer, Amanda K.	24	11	Suar22
0139-1757	29	3878400	SL2,SL1,LL2,LL1	0.4	0.4	0.4	0.4	2005-07-10	Houck, James R.	186	114	Cush06, Suar22
0144-0716	3136	10363136	SL2,SL1	12	12	2005-01-15	Cruz, Kelle	24	5	Suar22
0251-0352	3136	10364160	SL2,SL1	6	6	2005-01-14	Cruz, Kelle	25	5	Suar22
0255-4700	51	4192000	SL2,SL1,LL2,LL1	8	8	8	16	2004-01-07	Houck, James R.	54	35	Roel04
0355+1133	50059	25365504	SL2,SL1	48	48	2008-10-10	Burgasser, Adam J.	142	40	Fili15, Suar22
0415-0935	3431	10975232, 10975488, 12238080, 12238848	SL2,SL1	288	288	2005-09-06, 2005-09-07, 2005-09-12	Leggett, Sandy K.	18	44	Saum07
0423-0414	51	4195584, 12495360	SL2,SL1,LL2,LL1	24	32	8	16	2004-02-06, 2005-09-12	Houck, James R.	30	14	Cush06
0429-3123	3136	10364928	SL2,SL1	6	6	2005-02-10	Cruz, Kelle	73	26	Suar22
0439-2353	3136	10365184	SL2,SL1	14	14	2005-02-18	Cruz, Kelle	20	8	Fili15, Suar22
0445-3048	3136	10365440	SL2,SL1	12	12	2005-03-14	Cruz, Kelle	20	8	Fili15, Suar22
0501-0010	50059	25363968	SL2,SL1	62	64	2008-11-12	Burgasser, Adam J.	43	9	Fili15
0523-1403	3136	10365696	SL2,SL1	6	6	2005-03-12	Cruz, Kelle	26	7	Fili15, Suar22
0532+8246	51	12497408	SL2,SL1	16	16	2005-03-23	Houck, James R.	6	1	Suar22
0539-0059	51	4190720	SL2,SL1,LL2,LL1	16	16	8	8	2004-03-23	Houck, James R.	28	8	Cush06, Suar22
0559-1404	51	4183296, 4183040	SL2,SL1,LL2,LL1	32	32	8	16	2004-03-23, 2005-03-17	Houck, James R.	17	13	Cush06
0624-4521	3136	10365952	SL2,SL1	14	14	2005-03-20	Cruz, Kelle	28	12	Fili15, Suar22
0700+3157	3136	10366208	SL2,SL1	6	6	2005-04-21	Cruz, Kelle	32	8	Fili15, Suar22
0727+1710	20544	14825472	SL2,SL1	120	120	2006-04-18	Burgasser, Adam J.	11	13	Suar22
0746+2000	51	4186624	SL2,SL1,LL2,LL1	16	16	4	4	2004-03-27	Houck, James R.	60	32	Cush06, Suar22
0758+3247	3431	10978304	SL2,SL1	16	16	2004-10-24	Leggett, Sandy K.	21	12	Step09
0805+4812	3431	10979328	SL2,SL1	16	72	2004-10-23	Leggett, Sandy K.	14	9	Step09
0825+2115	51	4191232, 12497152	SL2,SL1,LL2,LL1	32	32	4	4	2004-04-20, 2005-11-15	Houck, James R.	28	8	Cush06
0829+2646	29	3876096	SL2,SL1	0.4	0.4	2004-04-20	Houck, James R.	64	26	Cush06
0830+4828	3136	13375744	SL2,SL1	16	16	2005-03-24	Cruz, Kelle	3	2	Suar22
0837-0000	51	4183552, 12495616	SL2,SL1	32	32	2004-04-13, 2005-04-23	Houck, James R.	2	2	Suar22
0857+5708	3431	10979584	SL2,SL1	8	8	2004-10-23	Leggett, Sandy K.	20	7	Step09
0908+5032	3431	10978816	SL2,SL1	8	16	2004-10-23	Leggett, Sandy K.	20	8	Step09
0911+7401	3136	10367488	SL2,SL1	6	6	2005-03-13	Cruz, Kelle	6	2	Suar22
0912+1459	51	12494080	SL2,SL1	16	16	2005-04-23	Houck, James R.	19	8	Cush06
0920+3517	51	4190976	SL2,SL1	16	16	2004-04-19	Houck, James R.	12	4	Suar22
0921-2104	3136	10368000	SL2,SL1	6	6	2005-05-31	Cruz, Kelle	24	7	Suar22
0929+3429	51	4195072	SL2,SL1	16	16	2004-04-19	Houck, James R.	8	2	Cush06, Suar22
0937+2931	51	4195328, 12494848	SL2,SL1	32	32	2004-04-18, 2005-11-17	Houck, James R.	18	17	Cush06
0939-2448	20544	14824704	SL2,SL1	120	120	2006-05-24	Burgasser, Adam J.	11	45	Burg08c
1013-1356	251	12435200	SL2,SL1	64	72	2005-06-07	Burgasser, Adam J.	10	1	Suar22

Table 2 – (Continued)

Dwarf (hhmm±ddmm)	Prog. ID	AOR KEY	Modules	Exposure Time				Obs. Date (UT; YYYY/MM/DD)	PI	S/N at		Publication Reference ¹
				SL2	SL1	LL2	LL1			(min)	6 μm	
											12 μm	
1017+1308	50367	26087680	SL2,SL1	14	54	2009-01-19	Cushing, Michael C.	10	5	Fili15, Suar22
1021-0304	51	4183808, 12497920	SL2,SL1	32	32	2004-05-13, 2005-06-07	Houck, James R.	5	4	Cush06, Suar22
1022+5825	3136	10368512	SL2,SL1	12	12	2005-04-16	Cruz, Kelle	4	1	Suar22
1028+5654	50667	26685952	SL1	...	200	2008-12-05	Albert, Loic	...	3	Suar22
1036-3441	51	12494592	SL2,SL1	16	16	2006-01-23	Houck, James R.	25	12	Fili15, Suar22
1045-0149	3136	10368768	SL2,SL1	6	6	2005-05-23	Cruz, Kelle	19	4	Suar22
1048+0111	3136	10369024	SL2,SL1	6	6	2005-05-23	Cruz, Kelle	21	5	Suar22
1051+5613	3136	10369280	SL2,SL1	6	6	2005-04-16	Cruz, Kelle	20	5	Suar22
1052+4422	20514	15492864	SL2,SL1	64	200	2006-05-23	Golimowski, David A.	16	12	Step09
1106+2754	24	16201728	SL2,SL1	16	16	2005-12-15	Roellig, Thomas	24	11	Kirk10, Suar22
1108+6830	51	4187648	SL2,SL1,LL2,LL1	16	16	4	4	2004-04-18	Houck, James R.	60	16	Cush06, Suar22
1110+0116	3431	10976768, 10977024, 12237568	SL2,SL1	144	288	2005-05-23, 2005-01-15	Leggett, Sandy K.	8	11	Step09
1112+3548	50367	26088192	SL2,SL1	12	22	2009-01-19	Cushing, Michael C.	18	5	Suar22
1114-2618	20544	14825216	SL2,SL1	120	120	2006-02-01	Burgasser, Adam J.	11	23	Suar22
1126-5003	50059	25361409	SL2,SL1	64	64	2009-04-05	Burgasser, Adam J.	39	12	Suar22
1155+0559	20514	14793216	SL2,SL1	32	96	2006-01-26	Golimowski, David A.	9	9	Step09
1207+0244	3431	12237824, 12238336	SL2,SL1	64	128	2005-06-06, 2005-06-03	Leggett, Sandy K.	19	14	Step09
1213-0432	3136	10370048	SL2,SL1	14	14	2005-06-06	Cruz, Kelle	16	3	Suar22
1217-0311	51	4184320	SL2,SL1	16	16	2005-01-03	Houck, James R.	3	3	Cush06, Suar22
1225-2739	51	12496128	SL2,SL1,LL2	16	16	32	...	2005-06-30	Houck, James R.	6	7	Cush06, Suar22
1237+6526	51	4184832	SL2,SL1	16	16	2004-03-03	Houck, James R.	4	3	Cush06, Suar22
1239+5515	51	4194304	SL2,SL1,LL2,LL1	16	16	4	4	2004-04-18	Houck, James R.	27	9	Cush06, Suar22
1254-0122	51	4185088, 12495872	SL2,SL1,LL2,LL1	32	32	8	16	2004-02-04, 2006-01-23	Houck, James R.	14	6	Cush06
1305-2541	51	4187904	SL2,SL1	16	16	2005-02-15	Houck, James R.	43	10	Cush06
1331-0116	20514	15492608	SL2,SL1	64	200	2006-01-28	Golimowski, David A.	10	6	Step09
1335+1130	40449	27513600	SL1	...	128	2008-08-09	Leggett, Sandy K.	...	6	Legg09
1425-3650	3136	10370816	SL2,SL1	6	6	2005-02-15	Cruz, Kelle	37	9	Fili15, Suar22
1439+1839	251	12433664	SL2,SL1	56	80	2005-07-01	Burgasser, Adam J.	22	9	Suar22
1439+1929	51	4187136	SL2,SL1	16	16	2005-07-06	Houck, James R.	41	11	Cush06
1441-0945	50367	26087936	SL2,SL1	19	54	2009-03-09	Cushing, Michael C.	10	5	Suar22
1448+1031	3136	10371072	SL2,SL1	14	14	2005-02-14	Cruz, Kelle	27	7	Fili15, Suar22
1456-2809	29	3876608	SL2,SL1,LL2,LL1	0.5	0.5	12	12	2004-02-29	Houck, James R.	33	11	Cush06
1457-2121	51	4186368	SL2,SL1	16	16	2005-02-15	Houck, James R.	10	13	Cush06
1503+2525	51	6314496	SL2,SL1	16	16	2005-07-06	Houck, James R.	16	14	Cush06
1506+1321	51	12496384	SL2,SL1	16	16	2005-07-09	Houck, James R.	39	12	Cush06
1507-1627	51	4190208	SL2,SL1	16	16	2005-08-08	Houck, James R.	58	17	Cush06
1515+4847	51	12494336	SL2,SL1	16	16	2005-03-19	Houck, James R.	32	14	Cush06
1516+3053	20514	15493120	SL2,SL1	80	200	2005-08-15	Golimowski, David A.	12	11	Step09
1520+3546	20514	14793984	SL2,SL1	32	96	2005-08-15	Golimowski, David A.	16	10	Step09
1523+3014	51	12497664	SL2,SL1	16	16	2005-03-19	Houck, James R.	16	7	Cush06, Suar22
1526+2043	51	4191488	SL2,SL1	16	16	2004-03-03	Houck, James R.	11	2	Cush06, Suar22
1610-0040	51	12496640	SL2,SL1	16	16	2005-08-07	Houck, James R.	24	5	Suar22
1615+3559	51	12495104	SL2,SL1	16	16	2005-02-16	Houck, James R.	16	4	Cush06, Suar22
1624+0029	51	4185600	SL2,SL1	16	16	2005-08-07	Houck, James R.	8	9	Cush06
1626+3925	251	13659392	SL2,SL1	64	72	2005-06-03	Burgasser, Adam J.	12	5	Suar22
1658+7027	51	4193024	SL2,SL1,LL2,LL1	16	16	4	4	2004-04-17	Houck, James R.	34	12	Cush06, Suar22

Table 2 – (Continued)

Dwarf	Prog. ID	AOR KEY	Modules	Exposure Time				Obs. Date (UT; YYYY/MM/DD)	PI	S/N at		Publication Reference ¹
				SL2	SL1	LL2	LL1	(min)		6 μm	12 μm	
(hhmm±ddmm)												
1707–0558	3136	10371584	SL2,SL1	6	6	2005-04-17	Cruz, Kelle	49	16	Suar22
1721+3344	50059	25365760	SL2,SL1	64	64	2008-08-01	Burgasser, Adam J.	49	12	Suar22
1728+3948	51	4191744	SL2,SL1	16	16	2004-04-16	Houck, James R.	17	5	Cush06 , Suar22
1731+2721	3136	10371840	SL2,SL1	6	6	2005-08-04	Cruz, Kelle	41	15	Suar22
1753–6559	3136	10372096	SL2,SL1	12	12	2005-09-08	Cruz, Kelle	18	5	Suar22
1807+5015	3136	10372352	SL2,SL1	6	6	2005-07-13	Cruz, Kelle	25	9	Suar22
1821+1414	51	16176128	SL2,SL1	16	16	2006-04-21	Houck, James R.	117	36	Loop08
1828+1229	24	16202240	SL2,SL1	14	14	2006-04-20	Roellig, Thomas	6	2	Kirk10 , Suar22
1916+0509	29	12486401	SL2,SL1,LL2,LL1	1	1	8	8	2005-10-11	Houck, James R.	52	19	Cush06
1936–5502	3136	10372608	SL2,SL1	14	14	2005-09-14	Cruz, Kelle	15	4	Suar22
2057–0252	3136	10373120	SL2,SL1	6	6	2005-05-25	Cruz, Kelle	23	4	Fili15 , Suar22
2132+1341	50367	26087168	SL2,SL1	62	158	2009-01-04	Cushing, Michael C.	12	7	Suar22
2139+0220	3136	12913664	SL2,SL1	8	8	2005-05-25	Cruz, Kelle	10	2	Fili15 , Suar22
2144+1446	40489	23795968, 23796224	SL2,SL1	256	448	2008-08-02, 2008-07-11	Metchev, Stanimir	26	385	Suar21
2146–0010	527	28721408, 28721920	SL1	...	336	2008-12-16	Burningham, Ben	...	6	Legg10b
2148+4003	24	16201984	SL2,SL1	16	16	2005-12-15	Roellig, Thomas	141	57	Loop08
2152+0937	3136	10373632	SL2,SL1	16	16	2005-07-09	Cruz, Kelle	18	5	Suar22
2204–5646	51	6313730	SL2,SL1,LL2,LL1	8	8	8	16	2005-05-31	Houck, James R.	75	66	Roel04
2224–0158	51	4189440	SL2,SL1	16	16	2004-11-13	Houck, James R.	37	8	Cush06
2238–1517	29	3878912	SL2,SL1,LL2,LL1	0.4	0.4	0.4	0.4	2004-06-07	Houck, James R.	158	76	Cush06 , Suar22
2244+2043	3431	10979840	SL2,SL1	16	48	2004-12-10	Leggett, Sandy K.	19	12	Step09
2254+3123	3431	12238592, 12239104, 12239360	SL2,SL1	88	288	2005-01-05	Leggett, Sandy K.	14	13	Step09
2351–2537	3136	10374144	SL2,SL1	6	6	2005-07-05	Cruz, Kelle	27	6	Fili15 , Suar22

Note. ¹A second reference (Suar22) is added when the target spectrum is not shown nor available in the first reference.

References. Burg08c: [Burgasser et al. \(2008c\)](#), Cus06: [Cushing et al. \(2006\)](#), Fili15: [Filippazzo et al. \(2015\)](#), Kirk10: [Kirkpatrick et al. \(2010\)](#), Legg09: [Leggett et al. \(2009\)](#), Legg10b: [Leggett et al. \(2010b\)](#), Loop08: [Looper et al. \(2008\)](#), Roel04: [Roellig et al. \(2004\)](#), Saum07: [Saumon et al. \(2007\)](#), Suar21: [Suárez et al. \(2021\)](#), Suar22: This work, Step09: [Stephens et al. \(2009\)](#).

(This table is available in machine-readable form in the online supplementary data.)

Table 3: Select properties and observing log of the 8 field $\geq M5$ dwarfs with *Spitzer* IRS observations that not yield detectable signal.

Designation	Other Name	R.A. _{J2000} ($^{\circ}$)	Decl. _{J2000} ($^{\circ}$)	Discovery Ref.	SpT _{opt}	Ref.	SpT _{IR}	Ref.
2MASS J01075242+0041563	...	16.9680	0.6991	Geba02	L8	Hawl02	L7p	Gagn15
2MASS J12095613-1004008	...	182.4840	-10.0671	Burg04b	T3.5	Kirk08	T3	Burg06b
2MASS J12281523-1547342	...	187.0635	-15.7930	Delf1997	L5	Kirk99	L6	Knap04
2MASS J13153094-2649513	...	198.8786	-26.8311	Hall2002	L5.5	Kirk08	L6.7	Bard14
2MASS J14243909+0917104	GD 165B	216.1629	9.2863	Beck1988	L4	Kirk99	L3	Knap04
2MASS J14250510+7102097	LSR J1425+7102	216.2709	71.0360	Lepi2003	sdM8	Lepi2003
2MASS J14304358+2915405	...	217.6816	29.2613	Wils03	L2	Cruz03	L1.5	Bard14
CFBDS J150000-182407	...	225.0014	-18.4021	Albe11	T4.5	Albe11

Prog. ID	AOR KEY	Modules	Exposure Time				Obs. Date (UT; YYYY/MM/DD)	PI
			SL2	SL1	LL2	LL1		
			(min)					
3136	12913920	SL2,SL1	8	8	0	0	2005-01-14	Cruz, Kelle
20514	14795264,14795520,14795776	SL2,SL1	144	288	0	0	2006-01-30, 2006-01-31, 2006-02-01	Golimowski, David A
50367	26088448	SL2,SL1	12	24	0	0	2009-03-06	Cushing, Michael C
20716	15034112	SL2,SL1	16	16	0	0	2006-03-05	Gizis, John E
122	5020672	SL2,SL1	1	1	0	0	2004-06-24	Gehrz, Robert
251	12435968,13659136	SL2,SL1	128	144	0	0	2005-02-10, 2005-06-04	Burgasser, Adam J
50367	26087424	SL2,SL1	20	56	0	0	2009-03-06	Cushing, Michael C
50667	27414016	SL1	0	159	0	0	2009-04-01	Albert, Loic

References. Albe11: Albert et al. (2011), Bard14: Bardalez Gagliuffi et al. (2014), Beck1988: Becklin & Zuckerman (1988), Burg04b: Burgasser et al. (2004), Burg06b: Burgasser et al. (2006b), Cruz03: Cruz et al. (2003), Delf1997: Delfosse et al. (1997), Gagné15: Gagné et al. (2015), Geba02: Geballe et al. (2002), Hall2002: Hall (2002), Hawl02: Hawley et al. (2002), Kirk99: Kirkpatrick et al. (1999), Kirk08: Kirkpatrick et al. (2008), Lepi2003: Lépine et al. (2003a), Knap04: Knapp et al. (2004), Wils03: Wilson et al. (2003).

Table 4: Published IRAC [8.0] and WISE W3 photometry, and corresponding synthetic magnitudes of the 113 field M5–T9 dwarfs with IRS spectra.

Dwarf (hhmm±ddmm)	IRAC [8.0] (mag)	IRAC Ref.	WISE W3 ^a (mag)	IRAC [8.0] ^b _{synt.} (mag)	WISE W3 ^b _{synt.} (mag)
0000+2554	12.500±0.030	Legg07	...	12.950±0.073	...
0004–4044	10.130±0.020	Patt06	9.803±0.048	10.413±0.136	...
0024–0158	9.550±0.010	Patt06	9.388±0.039	9.531±0.059	9.392±0.112
0025+4759	11.364±0.121	11.459±0.089	...
0034–0052	13.910±0.060	Warr07	11.955±0.000
0034+0523	12.250±0.110	Fili15	11.780±0.313	12.387±0.116	...
0036+1821	10.060±0.010	Patt06	9.851±0.054	9.996±0.043	9.846±0.092
0059–0114	...	Grif12	11.630±0.000
0136+0933	9.738±0.048	10.287±0.058	...
0139–1757	4.766±0.015	4.901±0.017	4.758±0.019
0144–0716	10.883±0.100	11.063±0.089	...
0251–0352	10.437±0.078	10.686±0.087	...
0255–4700	9.610±0.010	Patt06	9.142±0.027	9.621±0.027	9.176±0.035
0355+1133	9.219±0.035	9.437±0.020	...
0415–0935	12.110±0.050	Patt06	11.093±0.125	12.010±0.044	...
0423–0414	11.010±0.030	Patt06	10.558±0.089	11.026±0.044	10.619±0.089
0429–3123	9.067±0.028	9.223±0.026	...
0439–2353	11.280±0.090	Fili15	11.074±0.121	11.268±0.079	...
0445–3048	10.980±0.070	Fili15	10.709±0.080	10.982±0.071	...
0501–0010	11.030±0.030	Luhm09	10.746±0.106	11.369±0.052	...
0523–1403	10.700±0.080	Fili15	10.375±0.071	10.697±0.075	...
0532+8246	13.030±0.100	Patt06	12.367±0.000	13.574±0.367	...
0539–0059	11.200±0.040	Patt06	11.716±0.288	11.204±0.069	11.170±0.091
0559–1404	11.420±0.020	Patt06	10.605±0.089	11.387±0.076	10.550±0.113
0624–4521	10.970±0.070	Fili15	10.760±0.072	10.968±0.060	...
0700+3157	9.980±0.060	Fili15	9.717±0.051	9.954±0.063	...
0727+1710	12.640±0.110	Patt06	11.924±0.309	12.639±0.108	...
0746+2000	9.570±0.010	Patt06	9.402±0.042	9.554±0.022	9.428±0.038
0758+3247	11.330±0.050	Legg07	10.670±0.099	11.298±0.059	...
0805+4812	12.100±0.030	Legg07	11.916±0.328	12.233±0.083	...
0825+2115	10.930±0.020	Patt06	10.509±0.096	10.928±0.072	10.577±0.133
0829+2646	6.740±0.010	Patt06	6.618±0.016	6.712±0.028	...
0830+4828	11.598±0.256	13.035±0.324	...
0837–0000	14.220±0.140	Patt06	12.712±0.000	13.859±0.418	...
0857+5708	10.740±0.020	Patt06	10.317±0.063	10.995±0.091	...
0908+5032	11.130±0.030	Patt06	10.748±0.114	11.247±0.076	...
0911+7401	10.559±0.076	12.390±0.322	...
0912+1459	11.950±0.050	Patt06	11.297±0.189	11.954±0.082	...
0920+3517	12.210±0.220	Fili15	12.126±0.390	12.178±0.152	...
0921–2104	10.387±0.069	10.621±0.079	...
0929+3429	12.119±0.327	12.458±0.195	...
0937+2931	11.730±0.040	Patt06	10.696±0.101	11.653±0.065	...
0939–2448	11.890±0.030	Burg08c	10.667±0.086	11.868±0.057	...
1013–1356	12.359±0.000	13.476±0.218	...
1017+1308	11.700±0.030	Patt06	11.762±0.284	11.780±0.117	...
1021–0304	13.160±0.110	Patt06	12.286±0.424	13.313±0.229	...
1022+5825	11.156±0.137	13.071±0.434	...
1028+5654
1036–3441	11.890±0.140	Fili15	11.454±0.185	11.860±0.061	...
1045–0149	10.768±0.109	10.938±0.098	...
1048+0111	10.582±0.111	10.754±0.086	...
1051+5613	10.782±0.095	10.981±0.093	...
1052+4422	12.360±0.030	Legg07	12.530±0.420	12.428±0.069	...
1106+2754	11.526±0.195	11.784±0.063	...
1108+6830	10.168±0.049	10.348±0.031	10.175±0.058
1110+0116	13.210±0.160	Patt06	12.000±0.294	13.061±0.108	...
1112+3548	11.036±0.133	11.319±0.110	...
1114–2618	12.250±0.040	Legg10a	11.346±0.179	12.261±0.078	...
1126–5003	11.584±0.146	11.619±0.052	...
1155+0559	12.260±0.040	Legg07	11.968±0.331	12.163±0.090	...
1207+0244	12.230±0.060	Legg07	11.467±0.214	12.125±0.064	...
1213–0432	11.052±0.216	11.822±0.155	...

Table 4 – (Continued)

Dwarf (hhmm±ddmm)	IRAC [8.0] (mag)	IRAC Ref.	WISE W3 ^a (mag)	IRAC [8.0] ^b _{synt.} (mag)	WISE W3 ^b _{synt.} (mag)
1217–0311	12.950±0.180	Patt06	11.704±0.264	12.701±0.326	...
1225–2739	12.240±0.020	Patt06	11.157±0.146	12.307±0.201	11.255±0.219
1237+6526	12.780±0.110	Patt06	11.939±0.224	13.000±0.218	...
1239+5515	11.430±0.040	Fili15	11.108±0.095	11.357±0.067	11.054±0.116
1254–0122	11.750±0.040	Patt06	10.972±0.137	11.743±0.103	11.026±0.181
1305–2541	10.610±0.020	Patt06	10.418±0.064	10.559±0.046	...
1331–0116	12.620±0.060	Patt06	12.489±0.435	12.506±0.098	...
1335+1130	13.370±0.070	Burn08	12.151±0.358
1425–3650	10.110±0.050	Fili15	10.019±0.047	10.122±0.059	...
1439+1839	11.859±0.203	11.909±0.054	...
1439+1929	10.670±0.020	Patt06	10.523±0.057	10.635±0.046	...
1441–0945	12.110±0.338	11.809±0.128	...
1448+1031	11.060±0.080	Fili15	10.827±0.088	11.077±0.083	...
1456–2809	8.360±0.010	Patt06	8.273±0.025	8.336±0.050	8.254±0.071
1457–2121	11.970±0.070	Patt06	10.784±0.086	11.994±0.099	...
1503+2525	11.540±0.040	Grif12	10.709±0.071	11.422±0.080	...
1506+1321	10.580±0.010	Patt06	10.491±0.062	10.547±0.046	...
1507–1627	9.990±0.010	Patt06	9.685±0.048	9.976±0.035	...
1515+4847	10.830±0.020	Patt06	10.461±0.050	10.888±0.050	...
1516+3053	12.470±0.040	Legg07	12.093±0.203	12.513±0.064	...
1520+3546	12.260±0.030	Legg07	11.998±0.186	12.202±0.066	...
1523+3014	12.210±0.140	Fili15	11.905±0.181	12.279±0.088	...
1526+2043	12.320±0.040	Patt06	12.301±0.256	12.272±0.144	...
1610–0040	11.088±0.134	11.349±0.087	...
1615+3559	11.434±0.132	11.686±0.121	...
1624+0029	12.840±0.090	Patt06	12.163±0.394	12.789±0.145	...
1626+3925	12.174±0.000	12.826±0.115	...
1658+7027	10.844±0.058	11.084±0.052	10.854±0.108
1707–0558	9.399±0.045	9.586±0.036	...
1721+3344	11.400±0.020	Patt06	11.123±0.110	11.452±0.038	...
1728+3948	12.130±0.030	Patt06	11.743±0.150	12.156±0.121	...
1731+2721	9.875±0.043	9.996±0.039	...
1753–6559	11.032±0.099	11.406±0.115	...
1807+5015	10.505±0.056	10.667±0.068	...
1821+1414	9.928±0.052	10.097±0.023	...
1828+1229	12.683±0.505	13.052±0.269	...
1916+0509	8.140±0.000	Patt06	8.041±0.021	8.111±0.033	8.053±0.050
1936–5502	11.682±0.384	11.748±0.123	...
2057–0252	10.277±0.080	10.641±0.086	...
2132+1341	11.645±0.000	12.487±0.100	...
2139+0220	10.496±0.084	11.657±0.200	...
2144+1446	12.580±0.110	Luhm07a	11.777±0.217	12.526±0.042	...
2146–0010	14.360±0.080	Legg10a	12.312±0.000
2148+4003	9.631±0.042	9.841±0.019	...
2152+0937	11.207±0.172	11.544±0.098	...
2204–5646	8.980±0.040	Patt06	8.393±0.023	9.023±0.021	8.275±0.025
2224–0158	10.810±0.020	Patt06	10.540±0.101	10.861±0.061	...
2238–1517	5.005±0.015	5.306±0.018	5.291±0.022
2244+2043	11.360±0.030	Legg07	11.225±0.141	11.387±0.059	...
2254+3123	12.780±0.100	Patt06	12.111±0.340	12.823±0.065	...
2351–2537	10.262±0.073	10.523±0.072	...

Notes.^a WISE W3 photometry from Cutri et al. (2013).^b Synthetic magnitudes (corrected by the –0.064 mag mean offset with respect to the observations) from the IRS spectra.**References.** Burg08c: Burgasser et al. (2008c), Fili15: Filippazzo et al. (2015), Grif12: Griffith et al. (2012), Legg07: Leggett et al. (2007), Legg10a: Leggett et al. (2010a), Luhm07a: Luhman et al. (2007a), Luhm09: Luhman et al. (2009), Patt06: Patten et al. (2006), Warr07: Warren et al. (2007).

(This table is available in machine-readable form in the online supplementary data.)

Table 5: Spectral index values of the principal mid-infrared absorption bands for the 113 field M5–T9 dwarfs with IRS spectra.

Dwarf (hhmm±ddmm)	H ₂ O Index	CH ₄ Index	NH ₃ Index	Silicate Index
0000+2554	1.44±0.12	2.92±0.25	1.24±0.05	0.72±0.14
0004–4044	1.12±0.02	0.67±0.05	1.05±0.07	1.15±0.21
0024–0158	1.03±0.01	0.67±0.01	1.10±0.02	1.01±0.04
0025+4759	1.07±0.01	0.63±0.03	1.03±0.05	1.35±0.10
0034–0052	...	4.59±0.48	1.63±0.18	...
0034+0523	1.32±0.09	2.47±0.12	1.36±0.05	0.74±0.12
0036+1821	1.12±0.01	0.59±0.01	1.02±0.03	1.28±0.08
0059–0114	...	3.52±0.37	1.60±0.16	...
0136+0933	1.20±0.03	1.56±0.04	1.21±0.02	0.71±0.08
0139–1757	1.05±0.01	0.67±0.01	1.13±0.01	1.09±0.02
0144–0716	1.05±0.02	0.57±0.02	1.00±0.04	1.46±0.06
0251–0352	1.11±0.02	0.56±0.02	1.13±0.04	1.16±0.06
0255–4700	1.33±0.03	1.03±0.02	1.09±0.02	0.84±0.05
0355+1133	1.00±0.01	0.55±0.01	1.05±0.01	1.35±0.03
0415–0935	1.58±0.14	3.85±0.23	1.56±0.11	0.61±0.09
0423–0414	1.27±0.03	1.03±0.02	1.10±0.02	0.88±0.05
0429–3123	1.04±0.01	0.67±0.01	1.16±0.02	1.09±0.04
0439–2353	1.24±0.03	0.71±0.02	1.06±0.03	1.12±0.08
0445–3048	1.04±0.02	0.70±0.02	1.15±0.04	1.10±0.07
0501–0010	1.01±0.02	0.46±0.03	1.04±0.04	1.45±0.19
0523–1403	1.13±0.01	0.61±0.03	1.14±0.06	1.19±0.11
0532+8246	1.18±0.05	0.47±0.06	1.09±0.17	1.08±0.21
0539–0059	1.35±0.03	0.67±0.04	0.94±0.05	1.05±0.19
0559–1404	1.17±0.05	2.10±0.10	1.32±0.04	0.71±0.08
0624–4521	1.12±0.02	0.68±0.01	1.05±0.03	1.23±0.06
0700+3157	1.16±0.01	0.70±0.01	1.10±0.03	1.05±0.05
0727+1710	1.12±0.06	2.67±0.16	1.51±0.06	0.66±0.13
0746+2000	1.08±0.02	0.65±0.01	1.10±0.02	1.09±0.03
0758+3247	1.17±0.07	1.09±0.08	0.98±0.04	0.74±0.15
0805+4812	1.14±0.06	0.84±0.03	1.02±0.05	1.19±0.13
0825+2115	1.19±0.02	0.69±0.02	1.05±0.03	1.05±0.09
0829+2646	1.07±0.01	0.70±0.01	1.17±0.02	1.05±0.03
0830+4828	1.38±0.13	1.57±0.20	1.27±0.13	0.61±0.21
0837–0000	1.34±0.11	1.24±0.13	1.07±0.10	0.82±0.21
0857+5708	1.26±0.03	0.72±0.02	1.12±0.02	1.02±0.09
0908+5032	1.23±0.06	0.81±0.04	1.14±0.05	0.98±0.09
0911+7401	1.10±0.05	0.78±0.08	1.21±0.13	1.21±0.32
0912+1459	1.33±0.04	1.29±0.05	1.22±0.05	0.87±0.10
0920+3517	1.24±0.07	0.68±0.05	0.95±0.07	1.33±0.25
0921–2104	1.11±0.01	0.70±0.02	1.15±0.03	1.00±0.07
0929+3429	1.17±0.11	0.70±0.13	0.76±0.16	1.24±0.31
0937+2931	1.33±0.08	2.52±0.09	1.52±0.06	0.60±0.08
0939–2448	1.66±0.15	4.93±0.24	1.58±0.12	0.60±0.11
1013–1356	1.11±0.07	0.63±0.07	0.92±0.11	1.52±0.34
1017+1308	1.01±0.03	0.74±0.04	1.10±0.04	1.07±0.13
1021–0304	1.19±0.07	1.77±0.18	1.20±0.07	0.89±0.18
1022+5825	1.23±0.09	0.74±0.12	0.82±0.12	1.27±0.42
1028+5654	...	2.92±0.41	1.24±0.10	...
1036–3441	1.32±0.04	0.98±0.03	1.11±0.03	0.88±0.08
1045–0149	1.07±0.02	0.74±0.02	1.10±0.03	0.98±0.08
1048+0111	1.06±0.02	0.73±0.02	1.09±0.04	0.99±0.07
1051+5613	1.08±0.02	0.70±0.02	1.36±0.07	1.12±0.10
1052+4422	1.26±0.06	0.79±0.06	1.05±0.04	0.97±0.16
1106+2754	1.28±0.04	1.39±0.04	1.23±0.03	0.76±0.05
1108+6830	1.02±0.02	0.65±0.02	1.11±0.03	1.07±0.07
1110+0116	1.19±0.05	2.36±0.16	1.14±0.06	0.62±0.09
1112+3548	1.15±0.02	0.68±0.02	0.98±0.05	1.37±0.11
1114–2618	1.39±0.16	3.40±0.26	1.52±0.09	0.60±0.11
1126–5003	1.14±0.02	0.69±0.02	1.15±0.03	1.12±0.08
1155+0559	0.83±0.04	0.73±0.05	1.34±0.06	1.06±0.16
1207+0244	1.18±0.05	0.94±0.03	1.06±0.02	0.86±0.09
1213–0432	1.18±0.03	0.65±0.04	1.00±0.07	1.16±0.16

Table 5 – (Continued)

Dwarf (hhmm±ddmm)	H ₂ O Index	CH ₄ Index	NH ₃ Index	Silicate Index
1217–0311	1.28±0.12	3.03±0.24	1.71±0.13	0.77±0.15
1225–2739	1.32±0.10	2.66±0.18	1.55±0.08	0.65±0.09
1237+6526	1.19±0.10	1.61±0.26	1.30±0.14	0.91±0.25
1239+5515	1.20±0.03	0.63±0.03	1.17±0.06	1.68±0.22
1254–0122	1.29±0.06	1.75±0.11	1.23±0.05	0.63±0.11
1305–2541	1.08±0.01	0.61±0.01	1.09±0.03	1.15±0.05
1331–0116	1.25±0.08	0.73±0.03	1.02±0.03	1.02±0.13
1335+1130	...	6.00±1.12	1.56±0.13	...
1425–3650	1.04±0.01	0.55±0.01	1.08±0.03	1.36±0.06
1439+1839	1.06±0.03	0.66±0.02	1.05±0.04	1.11±0.11
1439+1929	1.09±0.01	0.74±0.02	1.14±0.03	1.04±0.05
1441–0945	1.15±0.05	0.84±0.06	1.29±0.11	0.97±0.20
1448+1031	1.15±0.01	0.58±0.02	0.96±0.03	1.37±0.10
1456–2809	1.06±0.01	0.69±0.02	1.19±0.02	1.10±0.04
1457–2121	1.32±0.10	4.29±0.18	1.52±0.07	0.59±0.09
1503+2525	1.24±0.05	2.51±0.11	1.47±0.05	0.68±0.07
1506+1321	1.07±0.01	0.56±0.01	1.08±0.02	1.25±0.05
1507–1627	1.24±0.02	0.73±0.01	1.07±0.02	1.12±0.04
1515+4847	1.28±0.02	0.80±0.02	1.09±0.02	0.95±0.06
1516+3053	1.37±0.11	0.98±0.06	1.19±0.05	0.76±0.11
1520+3546	1.30±0.09	1.09±0.06	1.17±0.04	0.78±0.09
1523+3014	1.21±0.03	1.01±0.04	1.13±0.04	0.85±0.09
1526+2043	1.29±0.08	0.84±0.07	1.08±0.10	0.92±0.19
1610–0040	1.01±0.01	0.68±0.03	1.05±0.04	1.15±0.08
1615+3559	1.09±0.02	0.55±0.02	1.19±0.07	1.30±0.13
1624+0029	1.24±0.09	2.44±0.12	1.43±0.06	0.62±0.08
1626+3925	0.95±0.05	0.69±0.05	1.08±0.08	1.08±0.13
1658+7027	1.09±0.02	0.74±0.02	1.04±0.04	0.97±0.07
1707–0558	1.08±0.01	0.70±0.01	1.10±0.02	1.10±0.04
1721+3344	1.10±0.02	0.62±0.02	1.11±0.03	1.19±0.09
1728+3948	1.09±0.05	0.74±0.05	1.06±0.08	1.22±0.18
1731+2721	1.04±0.01	0.72±0.01	1.17±0.02	1.00±0.04
1753–6559	1.06±0.02	0.50±0.02	0.91±0.04	1.51±0.18
1807+5015	1.05±0.01	0.65±0.02	1.13±0.03	1.16±0.07
1821+1414	1.16±0.01	0.61±0.01	1.00±0.01	1.38±0.03
1828+1229	1.09±0.05	0.70±0.06	1.10±0.11	1.05±0.16
1916+0509	1.08±0.01	0.68±0.01	1.16±0.03	1.06±0.02
1936–5502	1.21±0.03	0.70±0.04	1.09±0.08	1.21±0.12
2057–0252	1.06±0.02	0.69±0.03	1.11±0.05	1.05±0.12
2132+1341	1.15±0.05	0.66±0.04	1.04±0.05	1.27±0.14
2139+0220	1.22±0.04	0.99±0.07	0.99±0.06	0.72±0.13
2144+1446	1.18±0.04	1.65±0.06	1.24±0.03	0.69±0.06
2146–0010	...	5.53±0.85	1.38±0.12	...
2148+4003	1.08±0.01	0.57±0.01	0.97±0.01	1.58±0.04
2152+0937	1.29±0.03	0.73±0.03	1.11±0.04	1.10±0.08
2204–5646	1.32±0.04	1.89±0.05	1.32±0.03	0.67±0.05
2224–0158	1.10±0.02	0.57±0.02	0.96±0.02	1.48±0.11
2238–1517	1.04±0.01	0.60±0.02	1.16±0.02	1.16±0.06
2244+2043	1.15±0.03	0.49±0.02	0.92±0.04	1.42±0.15
2254+3123	1.30±0.06	1.64±0.08	1.26±0.05	0.82±0.11
2351–2537	1.08±0.01	0.69±0.02	1.23±0.03	1.06±0.07

(This table is available in machine-readable form in the online supplementary data.)

REFERENCES

- Adame L., et al., 2011, *ApJ*, **726**, L3
- Albert L., Artigau É., Delorme P., Reylé C., Forveille T., Delfosse X., Willott C. J., 2011, *AJ*, **141**, 203
- Allard F., Hauschildt P. H., Alexander D. R., Tamai A., Schweitzer A., 2001, *ApJ*, **556**, 357
- Aller K. M., et al., 2016, *ApJ*, **821**, 120
- Allers K. N., Liu M. C., 2013, *ApJ*, **772**, 79
- Apai D., Pasquetti I., Bouwman J., Natta A., Henning T., Dullemond C. P., 2005, *Science*, **310**, 834
- Apai D., Radigan J., Buenzli E., Burrows A., Reid I. N., Jayawardhana R., 2013, *ApJ*, **768**, 121
- Artigau É., Doyon R., Lafrenière D., Nadeau D., Robert J., Albert L., 2006, *ApJ*, **651**, L57
- Artigau É., Bouchard S., Doyon R., Lafrenière D., 2009, *ApJ*, **701**, 1534
- Bailer-Jones C. A. L., 2004, *A&A*, **419**, 703
- Bailer-Jones C. A. L., Lamm M., 2003, *MNRAS*, **339**, 477
- Bailer-Jones C. A. L., Mundt R., 2001, *A&A*, **367**, 218
- Bardalez Gagliuffi D. C., et al., 2014, *ApJ*, **794**, 143
- Bartlett J. L., et al., 2017, *AJ*, **154**, 151
- Becklin E. E., Zuckerman B., 1988, *Nature*, **336**, 656
- Bernat D., et al., 2010, *ApJ*, **715**, 724
- Bessell M. S., 1991, *AJ*, **101**, 662
- Best W. M. J., et al., 2018, *ApJS*, **234**, 1
- Best W. M. J., Liu M. C., Magnier E. A., Dupuy T. J., 2021, *AJ*, **161**, 42
- Biller B., 2017, *The Astronomical Review*, **13**, 1
- Boeshaar P. C., 1976, PhD thesis, Ohio State University, Columbus.
- Bouwman J., Lawson W. A., Dominik C., Feigelson E. D., Henning T., Tielens A. G. G. M., Waters L. B. F. M., 2006, *ApJ*, **653**, L57
- Bouy H., Brandner W., Martín E. L., Delfosse X., Allard F., Basri G., 2003, *AJ*, **126**, 1526
- Bouy H., et al., 2008, *A&A*, **486**, 877
- Briceño C., Calvet N., Hernández J., Vivas A. K., Hartmann L., Downes J. J., Berlin P., 2005, *AJ*, **129**, 907
- Buenzli E., Apai D., Radigan J., Reid I. N., Flateau D., 2014, *ApJ*, **782**, 77
- Burgasser A. J., 2004, *ApJ*, **614**, L73
- Burgasser A. J., et al., 1999, *ApJ*, **522**, L65
- Burgasser A. J., et al., 2000a, *AJ*, **120**, 1100
- Burgasser A. J., et al., 2000b, *ApJ*, **531**, L57
- Burgasser A. J., et al., 2002, *ApJ*, **564**, 421
- Burgasser A. J., Kirkpatrick J. D., McElwain M. W., Cutri R. M., Burgasser A. J., Skrutskie M. F., 2003a, *AJ*, **125**, 850
- Burgasser A. J., Kirkpatrick J. D., Reid I. N., Brown M. E., Miskey C. L., Gizis J. E., 2003b, *ApJ*, **586**, 512
- Burgasser A. J., et al., 2003c, *ApJ*, **592**, 1186
- Burgasser A. J., Kirkpatrick J. D., Liebert J., Burrows A., 2003d, *ApJ*, **594**, 510
- Burgasser A. J., McElwain M. W., Kirkpatrick J. D., Cruz K. L., Tinney C. G., Reid I. N., 2004, *AJ*, **127**, 2856
- Burgasser A. J., Kirkpatrick J. D., Lowrance P. J., 2005a, *AJ*, **129**, 2849
- Burgasser A. J., Reid I. N., Leggett S. K., Kirkpatrick J. D., Liebert J., Burrows A., 2005b, *ApJ*, **634**, L177
- Burgasser A. J., Kirkpatrick J. D., Cruz K. L., Reid I. N., Leggett S. K., Liebert J., Burrows A., Brown M. E., 2006a, *ApJS*, **166**, 585
- Burgasser A. J., Geballe T. R., Leggett S. K., Kirkpatrick J. D., Golimowski D. A., 2006b, *ApJ*, **637**, 1067
- Burgasser A. J., Burrows A., Kirkpatrick J. D., 2006c, *ApJ*, **639**, 1095
- Burgasser A. J., Cruz K. L., Kirkpatrick J. D., 2007, *ApJ*, **657**, 494
- Burgasser A. J.,Looper D. L., Kirkpatrick J. D., Cruz K. L., Swift B. J., 2008a, *ApJ*, **674**, 451
- Burgasser A. J., Liu M. C., Ireland M. J., Cruz K. L., Dupuy T. J., 2008b, *ApJ*, **681**, 579
- Burgasser A. J., Tinney C. G., Cushing M. C., Saumon D., Marley M. S., Bennett C. S., Kirkpatrick J. D., 2008c, *ApJ*, **689**, L53
- Burgasser A. J., Cruz K. L., Cushing M., Gelino C. R.,Looper D. L., Faherty J. K., Kirkpatrick J. D., Reid I. N., 2010, *ApJ*, **710**, 1142
- Burningham B., et al., 2008, *MNRAS*, **391**, 320
- Burningham B., et al., 2009, *MNRAS*, **395**, 1237
- Burningham B., et al., 2021, *MNRAS*, **506**, 1944
- Burrows A., et al., 1997, *ApJ*, **491**, 856
- Calvet N., Briceño C., Hernández J., Hoyer S., Hartmann L., Sicilia-Aguilar A., Megeath S. T., D'Alessio P., 2005, *AJ*, **129**, 935
- Chiu K., Fan X., Leggett S. K., Golimowski D. A., Zheng W., Geballe T. R., Schneider D. P., Brinkmann J., 2006, *AJ*, **131**, 2722
- Clarke F. J., Tinney C. G., Covey K. R., 2002a, *MNRAS*, **332**, 361
- Clarke F. J., Oppenheimer B. R., Tinney C. G., 2002b, *MNRAS*, **335**, 1158
- Cohen J., 1988, *Statistical Power Analysis for the Behavioral Sciences* (Hillsdale, NJ: L. Erlbaum Associates)
- Cruz K. L., Reid I. N., Liebert J., Kirkpatrick J. D., Lowrance P. J., 2003, *AJ*, **126**, 2421
- Cruz K. L., et al., 2007, *AJ*, **133**, 439
- Cruz K. L., Kirkpatrick J. D., Burgasser A. J., 2009, *AJ*, **137**, 3345
- Cushing M. C., et al., 2006, *ApJ*, **648**, 614
- Cushing M. C., et al., 2008, *ApJ*, **678**, 1372
- Cushing M. C., et al., 2011, *ApJ*, **743**, 50
- Cutri R. M., et al., 2013, *yCat*, **2328**, 0
- Dahn C. C., et al., 2002, *AJ*, **124**, 1170
- Dahn C. C., et al., 2008, *ApJ*, **686**, 548
- Delfosse X., et al., 1997, *A&A*, **327**, L25
- Delorme P., et al., 2008, *A&A*, **482**, 961
- Dieterich S. B., Henry T. J., Jao W.-C., Winters J. G., Hosey A. D., Riedel A. R., Subasavage J. P., 2014, *AJ*, **147**, 94
- Downes J. J., et al., 2014, *MNRAS*, **444**, 1793
- Draine B. T., Lee H. M., 1984, *ApJ*, **285**, 89
- Dupuy T. J., Kraus A. L., 2013, *Science*, **341**, 1492
- Dupuy T. J., Liu M. C., 2012, *ApJS*, **201**, 19
- Dupuy T. J., Liu M. C., Leggett S. K., Ireland M. J., Chiu K., Golimowski D. A., 2015, *ApJ*, **805**, 56
- EROS Collaboration et al., 1999, *A&A*, **351**, L5
- Fan X., et al., 2000, *AJ*, **119**, 928
- Filippazzo J. C., Rice E. L., Faherty J., Cruz K. L., Van Gordon M. M., Looper D. L., 2015, *ApJ*, **810**, 158
- Folkes S. L., Pinfield D. J., Kendall T. R., Jones H. R. A., 2007, *MNRAS*, **378**, 901
- Forrest W. J., et al., 2004, *ApJS*, **154**, 443
- Furlan E., et al., 2005, *ApJ*, **621**, L129
- Furlan E., et al., 2006, *ApJS*, **165**, 568
- Furlan E., et al., 2008, *ApJS*, **176**, 184
- Furlan E., et al., 2011, *ApJS*, **195**, 3
- Gagné J., et al., 2015, *ApJS*, **219**, 33
- Gagné J., et al., 2017, *ApJ*, **841**, L1
- Geballe T. R., et al., 2002, *ApJ*, **564**, 466
- Gelino C. R., Marley M. S., Holtzman J. A., Ackerman A. S., Lodders K., 2002, *ApJ*, **577**, 433
- Girardin F., Artigau É., Doyon R., 2013, *ApJ*, **767**, 61
- Gizis J. E., 1997, *AJ*, **113**, 806
- Gizis J. E., 2002, *ApJ*, **575**, 484
- Gizis J. E., Monet D. G., Reid I. N., Kirkpatrick J. D., Liebert J., Williams R. J., 2000, *AJ*, **120**, 1085
- Gizis J. E., Reid I. N., Knapp G. R., Liebert J., Kirkpatrick J. D., Koerner D. W., Burgasser A. J., 2003, *AJ*, **125**, 3302
- Golimowski D. A., et al., 2004, *AJ*, **128**, 1733
- Griffith R. L., et al., 2012, *AJ*, **144**, 148
- Hall P. B., 2002, *ApJ*, **564**, L89
- Hanner M. S., Lynch D. K., Russell R. W., 1994, *ApJ*, **425**, 274
- Harding L. K., Hallinan G., Konopacky Q. M., Kratter K. M., Boyle R. P., Butler R. F., Golden A., 2013, *A&A*, **554**, A113
- Hawley S. L., et al., 2002, *AJ*, **123**, 3409
- Helling C., Thi W. F., Woitke P., Fridlund M., 2006, *A&A*, **451**, L9
- Henry T. J., Kirkpatrick J. D., 1990, *ApJ*, **354**, L29
- Houck J. R., et al., 2004, *ApJS*, **154**, 18
- Irwin M., McMahon R. G., Reid N., 1991, *MNRAS*, **252**, 61P
- Kao M. M., Hallinan G., Pineda J. S., Stevenson D., Burgasser A., 2018, *ApJS*, **237**, 25

- Karalidi T., Marley M., Fortney J. J., Morley C., Saumon D., Lupu R., Visscher C., Freedman R., 2021, *ApJ*, **923**, 269
- Kendall T. R., Delfosse X., Martín E. L., Forveille T., 2004, *A&A*, **416**, L17
- Kirkpatrick J. D., Henry T. J., McCarthy Donald W. J., 1991, *ApJS*, **77**, 417
- Kirkpatrick J. D., Henry T. J., Simons D. A., 1995, *AJ*, **109**, 797
- Kirkpatrick J. D., et al., 1999, *ApJ*, **519**, 802
- Kirkpatrick J. D., et al., 2000, *AJ*, **120**, 447
- Kirkpatrick J. D., Dahn C. C., Monet D. G., Reid I. N., Gizis J. E., Liebert J., Burgasser A. J., 2001, *AJ*, **121**, 3235
- Kirkpatrick J. D., et al., 2008, *ApJ*, **689**, 1295
- Kirkpatrick J. D., et al., 2010, *ApJS*, **190**, 100
- Knapp G. R., et al., 2004, *AJ*, **127**, 3553
- Koen C., 2003, *MNRAS*, **346**, 473
- Koen C., 2013, *MNRAS*, **428**, 2824
- Koen C., Matsunaga N., Menzies J., 2004, *MNRAS*, **354**, 466
- Leggett S. K., Allard F., Berriman G., Dahn C. C., Hauschildt P. H., 1996, *ApJS*, **104**, 117
- Leggett S. K., et al., 2000, *ApJ*, **536**, L35
- Leggett S. K., Saumon D., Marley M. S., Geballe T. R., Golimowski D. A., Stephens D., Fan X., 2007, *ApJ*, **655**, 1079
- Leggett S. K., et al., 2009, *ApJ*, **695**, 1517
- Leggett S. K., et al., 2010a, *ApJ*, **710**, 1627
- Leggett S. K., Saumon D., Birmingham B., Cushing M. C., Marley M. S., Pinfield D. J., 2010b, *ApJ*, **720**, 252
- Leinert C., Jahreiß H., Haas M., 1986, *A&A*, **164**, L29
- Lépine S., Shara M. M., Rich R. M., 2003a, *ApJ*, **585**, L69
- Lépine S., Rich R. M., Shara M. M., 2003b, *ApJ*, **591**, L49
- Liebert J., Kirkpatrick J. D., Cruz K. L., Reid I. N., Burgasser A., Tinney C. G., Gizis J. E., 2003, *AJ*, **125**, 343
- Liu M. C., Leggett S. K., 2005, *ApJ*, **634**, 616
- Liu M. C., Dupuy T. J., Allers K. N., 2013, *Astronomische Nachrichten*, **334**, 85
- Liu M. C., Dupuy T. J., Allers K. N., 2016, *ApJ*, **833**, 96
- Lodders K., 2002, *ApJ*, **577**, 974
- Lodieu N., Scholz R. D., McCaughrean M. J., Ibata R., Irwin M., Zinnecker H., 2005, *A&A*, **440**, 1061
- Looper D. L., Kirkpatrick J. D., Burgasser A. J., 2007, *AJ*, **134**, 1162
- Looper D. L., et al., 2008, *ApJ*, **686**, 528
- Lothringer J. D., et al., 2022, *Nature Astronomy*, **604**, 49
- Luhman K. L., et al., 2007a, *ApJ*, **654**, 570
- Luhman K. L., et al., 2007b, *ApJ*, **666**, 1219
- Luhman K. L., Mamajek E. E., Allen P. R., Cruz K. L., 2009, *ApJ*, **703**, 399
- Luyten W. J., 1949, *ApJ*, **109**, 532
- Mainzer A. K., et al., 2007, *ApJ*, **662**, 1245
- Manoj P., et al., 2011, *ApJS*, **193**, 11
- Marley M. S., Seager S., Saumon D., Lodders K., Ackerman A. S., Freedman R. S., Fan X., 2002, *ApJ*, **568**, 335
- Marley M. S., Saumon D., Goldblatt C., 2010, *ApJ*, **723**, L117
- Marocco F., et al., 2013, *AJ*, **146**, 161
- Marocco F., et al., 2015, *MNRAS*, **449**, 3651
- Martín E. L., Delfosse X., Basri G., Goldman B., Forveille T., Zapatero Osorio M. R., 1999, *AJ*, **118**, 2466
- Martín E. L., Zapatero Osorio M. R., Lehto H. J., 2001, *ApJ*, **557**, 822
- McCaughrean M. J., Close L. M., Scholz R.-D., Lenzen R., Biller B., Brandner W., Hartung M., Lodieu N., 2004, *A&A*, **413**, 1029
- McClure M. K., et al., 2010, *ApJS*, **188**, 75
- McElwain M. W., Burgasser A. J., 2006, *AJ*, **132**, 2074
- Merín B., et al., 2007, *ApJ*, **661**, 361
- Metchev S. A., et al., 2015, *ApJ*, **799**, 154
- Miles-Páez P. A., Pallé E., Zapatero Osorio M. R., 2017a, *MNRAS*, **472**, 2297
- Miles-Páez P. A., Metchev S. A., Heinze A., Apai D., 2017b, *ApJ*, **840**, 83
- Morales-Calderón M., et al., 2006, *ApJ*, **653**, 1454
- Morrow A. L., et al., 2008, *ApJ*, **676**, L143
- Olofsson J., et al., 2009, *A&A*, **507**, 327
- Pascucci I., Apai D., Luhman K., Henning T., Bouwman J., Meyer M. R., Lahuis F., Natta A., 2009, *ApJ*, **696**, 143
- Patten B. M., et al., 2006, *ApJ*, **651**, 502
- Pineda J. S., Hallinan G., Kirkpatrick J. D., Cotter G., Kao M. M., Mooley K., 2016, *ApJ*, **826**, 73
- Pokorny R. S., Jones H. R. A., Hambley N. C., Pinfield D. J., 2004, *A&A*, **421**, 763
- Pope B., Martinache F., Tuthill P., 2013, *ApJ*, **767**, 110
- Radigan J., Jayawardhana R., Lafrenière D., Artigau É., Marley M., Saumon D., 2012, *ApJ*, **750**, 105
- Radigan J., Lafrenière D., Jayawardhana R., Artigau E., 2014, *ApJ*, **793**, 75
- Reid I. N., Kirkpatrick J. D., Gizis J. E., Dahn C. C., Monet D. G., Williams R. J., Liebert J., Burgasser A. J., 2000, *AJ*, **119**, 369
- Reid I. N., Gizis J. E., Kirkpatrick J. D., Koerner D. W., 2001, *AJ*, **121**, 489
- Reid I. N., Lewitus E., Allen P. R., Cruz K. L., Burgasser A. J., 2006, *AJ*, **132**, 891
- Reid I. N., Cruz K. L., Kirkpatrick J. D., Allen P. R., Mungall F., Liebert J., Lowrance P., Sweet A., 2008, *AJ*, **136**, 1290
- Riaz B., 2009, *ApJ*, **701**, 571
- Riaz B., Gizis J. E., 2008, *ApJ*, **681**, 1584
- Riaz B., Lodieu N., Gizis J. E., 2009, *ApJ*, **705**, 1173
- Rilinger A. M., Espaillat C. C., 2021, arXiv e-prints, p. [arXiv:2106.05247](https://arxiv.org/abs/2106.05247)
- Roellig T. L., et al., 2004, *ApJS*, **154**, 418
- Ruiz M. T., Leggett S. K., Allard F., 1997, *ApJ*, **491**, L107
- Saumon D., Marley M. S., Lodders K., 2003, arXiv e-prints, pp. [astro-ph/0310805](https://arxiv.org/abs/astro-ph/0310805)
- Saumon D., et al., 2007, *ApJ*, **656**, 1136
- Schneider A. C., Cushing M. C., Kirkpatrick J. D., Mace G. N., Gelino C. R., Faherty J. K., Fajardo-Acosta S., Sheppard S. S., 2014, *AJ*, **147**, 34
- Scholz R.-D., McCaughrean M. J., Lodieu N., Kuhlbrotz B., 2003, *A&A*, **398**, L29
- Scholz R. D., Lehmann I., Matute I., Zinnecker H., 2004, *A&A*, **425**, 519
- Scholz A., Jayawardhana R., Wood K., Meeus G., Stelzer B., Walker C., O'Sullivan M., 2007, *ApJ*, **660**, 1517
- Sicilia-Aguilar A., Henning T., Juhász A., Bouwman J., Garmire G., Garmire A., 2008, *ApJ*, **687**, 1145
- Siegle N., Close L. M., Burgasser A. J., Cruz K. L., Marois C., Macintosh B., Barman T., 2007, *AJ*, **133**, 2320
- Stephens D. C., et al., 2009, *ApJ*, **702**, 154
- Strauss M. A., et al., 1999, *ApJ*, **522**, L61
- Stumpf M. B., Brandner W., Henning T., Bouy H., Koehler R., Hormuth F., Joergens V., Kasper M., 2008, arXiv e-prints, p. [arXiv:0811.0556](https://arxiv.org/abs/0811.0556)
- Suárez G., Metchev S., Leggett S. K., Saumon D., Marley M. S., 2021, *ApJ*, **920**, 99
- Tannock M. E., et al., 2021, *AJ*, **161**, 224
- Thorstensen J. R., Kirkpatrick J. D., 2003, *PASP*, **115**, 1207
- Tinney C. G., Burgasser A. J., Kirkpatrick J. D., McElwain M. W., 2005, *AJ*, **130**, 2326
- Van Biesbroeck G., 1961, *AJ*, **66**, 528
- Vos J. M., Allers K. N., Biller B. A., Liu M. C., Dupuy T. J., Gallimore J. F., Adenuga I. J., Best W. M. J., 2018, *MNRAS*, **474**, 1041
- Vos J. M., et al., 2020, *AJ*, **160**, 38
- Vos J. M., Faherty J. K., Gagné J., Marley M., Metchev S., Gizis J., Rice E. L., Cruz K., 2022, *ApJ*, **924**, 68
- Warren S. J., et al., 2007, *MNRAS*, **381**, 1400
- Werner M. W., et al., 2004, *ApJS*, **154**, 1
- Wilson J. C., Kirkpatrick J. D., Gizis J. E., Skrutskie M. F., Monet D. G., Houck J. R., 2001, *AJ*, **122**, 1989
- Wilson J. C., Miller N. A., Gizis J. E., Skrutskie M. F., Houck J. R., Kirkpatrick J. D., Burgasser A. J., Monet D. G., 2003, in Martín E., ed., IAU Symposium Vol. 211, Brown Dwarfs. p. 197
- Wilson P. A., Rajan A., Patience J., 2014, *A&A*, **566**, A111
- Zhang Z., Liu M. C., Best W. M. J., Dupuy T. J., Siverd R. J., 2021, arXiv e-prints, p. [arXiv:2102.05045](https://arxiv.org/abs/2102.05045)
- Zhou Y., et al., 2018, *AJ*, **155**, 132

This paper has been typeset from a TeX/LaTeX file prepared by the author.